Classical quantum friction at water–carbon interfaces

Anna T. Bui,[1] Fabian L. Thiemann,[2, 1, 3] Angelos Michaelides,[1] and Stephen J. Cox[1, a)]

[1)] *Yusuf Hamied Department of Chemistry, University of Cambridge, Lensfield Road, Cambridge, CB2 1EW, United Kingdom*

[2)] *Thomas Young Centre, London Centre for Nanotechnology, and Department of Physics and Astronomy, University College London, Gower Street, London, WC1E 6BT, United Kingdom*

[3)] *Department of Chemical Engineering, Sargent Centre for Process Systems Engineering, Imperial College London, South Kensington Campus, London, SW7 2AZ, United Kingdom*

Abstract: Friction at water–carbon interfaces remains a major puzzle with theories and simulations unable to explain experimental trends in nanoscale waterflow. A recent theoretical framework—quantum friction (QF)—proposes to resolve these experimental observations by considering nonadiabatic coupling between dielectric fluctuations in water and graphitic surfaces. Here, using a classical model that enables fine-tuning of the solid's dielectric spectrum, we provide evidence from simulations in general support of QF. In particular, as features in the solid's dielectric spectrum begin to overlap with water's librational and Debye modes, we find an increase in friction in line with that proposed by QF. At the microscopic level, we find that this contribution to friction manifests more distinctly in the dynamics of the solid's charge density than that of water. Our findings suggest that experimental signatures of QF may be more pronounced in the solid's response rather than liquid water's.

Recent advances in nanofluidics[1,2] show great promise for membrane-based desalination technologies[3–5] and energy harvesting applications.[6–11] Owing to the relative ease of fabricating carbon-based nanostructures, a feature common to many of these technologies is the presence of extended interfaces between liquid water and carbon. Despite significant research effort, there are still major gaps[12–15] in our understanding of water at graphitic surfaces.

Of particular curiosity, experiments have found that friction of water on carbon surfaces is ultra-low compared to other two-dimensional materials.[16–20] In addition, friction of water is much higher on multilayer graphite[21–23] than monolayer graphene[24] and a peculiar radius dependence in multi-walled carbon nanotubes[25,26] is observed. Reproducing these observations has so far remained beyond the realms of molecular simulations,[27–30] even with highly accurate interatomic potentials.[31] Consequently, these observations cannot be explained by the traditional "surface roughness" approach[32,33] that underpins much of our understanding of friction at liquid–solid interfaces.

A recent theoretical study[34] by Kavokine *et al.* has sought to explain the differences in friction at graphene vs. graphite by accounting for coupling between collective charge excitations of the liquid and the dynamics of electrons in the carbon substrate. In this framework of "quantum friction" (QF), friction of water on graphite is argued to be larger than that on graphene due to the presence of a dispersionless surface plasmon mode in graphite[35–37] that overlaps with liquid water's terahertz (THz) dielectric fluctuations.[38–40] The purpose of the present article is to explore QF with molecular simulations.

Such coupling between electronic motion in the solid and charge density fluctuations in the liquid is an effect beyond the Born–Oppenheimer approximation.[41] While simulation schemes to account for such nonadiabatic dynamics ("electronic friction") exist,[42–44] they rely on the accurate construction of a $(3N \times 3N)$ friction tensor, where N is the total number of atoms explicitly considered in the dynamics. So far, their application has been limited to single gas-phase molecules on metal surfaces,[45–48] where the friction coefficient on each atom can be well-approximated to depend only on the solid electron density locally.[49,50] The low-frequency dielectric modes of water, which are essential to the description of QF, however, are inherently collective in nature, prohibiting the application of these sophisticated methods at present.

While accurately accounting for nonadiabatic electronic motion is computationally challenging, low-frequency dielectric response of water is reasonably well captured by simple point charge models.[51,52] In this article, we therefore focus on this aspect of QF—that dissipative friction forces are mediated through a complex interplay of charge density fluctuations—which is more amenable to classical molecular dynamics (MD) simulations. By extending a standard treatment for polarizability in graphene such that its dielectric fluctuations can be precisely controlled, we will show that coupling between charge density fluctuations in the solid and liquid increases friction in line with the predictions of QF. Also similar to QF, this additional contribution is distinct from the typical surface roughness picture for friction. The insights afforded by our simulations suggest that microscopic signatures of QF manifest more distinctly in the dynamics of the solid's dielectric fluctuations rather than in the structure or dynamics of liquid water.

Model of the liquid–solid interface. The system
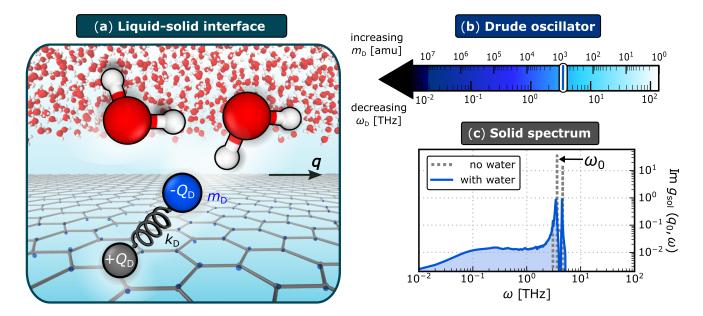
a)Electronic mail: sjc236@cam.ac.uk

Figure 1. **Model of the liquid–solid interface.** (a) Schematic illustrating the interface of a film of water on a graphene sheet. The graphene's charge density is described by a classical Drude oscillator model: each C atom carries a charge $+Q_D$ and is attached to a fictitious Drude particle of mass m_D and charge $-Q_D$ via a harmonic spring with force constant k_D. O, H, C atoms and Drude particles are in red, white, grey and blue, respectively. For clarity, only one Drude particle is highlighted and its displacement from the C atom is exaggerated (see SI for the actual distribution). The characteristic frequency of the Drude oscillators, $\omega_D = (k_D/m_D)^{1/2}$ is controlled by varying m_D, as indicated by the colorbar in (b). (c) In the absence of water, the surface response function of the solid, $g_{sol}(q_0, \omega)$ (shown for $\omega_D = 3.3$ THz), is dominated by two peaks, with ω_0 describing the position of the lower frequency peak. In the present case, $\omega_0 \approx 3.5$ THz $\approx \omega_D$, indicating a weak coupling between the Drude oscillators. With water present, these peaks are broadened.

we consider consists of a thin film of water on a frozen flat graphene sheet, as shown schematically in Fig. 1(a). To model water, we use the SPC/E model,[53] which reasonably captures both the librational modes (hindered molecular rotations) as a sharp peak at $\omega_{lib} \approx 20$ THz, and the Debye modes (hindered molecular translations) as a broad feature spanning $\sim 10^{-2} - 10^1$ THz.[51,52] Water–carbon interactions are modeled with a Lennard-Jones potential that reproduces the contact angle of water droplets on graphitic surfaces;[54] while such a potential captures the essential features of surface roughness contributions to friction, it lacks any dielectric response. For each carbon center we therefore also ascribe a charge $+Q_D$, and attach to it, via a harmonic spring with force constant k_D, a "Drude particle" of mass m_D and charge $-Q_D$. This classical Drude oscillator model is a common approach for modeling electronic polarizability,[55] and introduces electrostatic interactions between both the water film and the substrate, and the substrate with itself. In the absence of water, the graphene sheet can be considered a set of weakly interacting harmonic oscillators (see SI).

To parameterize the model, we set $Q_D = 1.852\,e$ and $k_D = 4184$ kJ mol^{-1}Å^{-2}, which have been shown to recover the polarizability tensor of a periodic graphene lattice.[56] In usual treatments of electronic polarizability, one follows a Car–Parrinello-like scheme[57] whereby

m_D is chosen to be sufficiently small to ensure adiabatic separation of the Drude and nuclear (in this case, water) motions. Here, we are inspired by the fact that, even for bulk systems, increasing m_D leads to nuclear motion experiencing drag forces.[58] We therefore treat m_D as a free parameter that tunes the frequency $\omega_D = (k_D/m_D)^{1/2}$ of an individual oscillator, anticipating that this may lead to an increase in friction at the liquid–solid interface. However, the details of how friction may vary with ω_D are not *a priori* obvious. In practice, we choose $1 \lesssim m_D/\text{amu} \lesssim 10^7$, such that $10^{-2} \lesssim \omega_D/\text{THz} \lesssim 10^2$ as indicated in Fig. 1(b). Importantly, changing m_D in this manner does not affect the system's static equilibrium properties.

In QF, significant overlap between the substrate and water is due to a dispersionless plasmon mode present in graphite but not graphene. While we cannot reasonably expect the classical Drude model to faithfully describe this plasmonic behavior, we can ask a more general question concerning how friction is affected when the substrate and fluid spectra overlap significantly. This question can readily be addressed by tuning m_D, as we describe above, without the need to introduce multilayer graphite. For simplicity, and ease of comparison between systems, we therefore employ a single graphene sheet in all simulations.

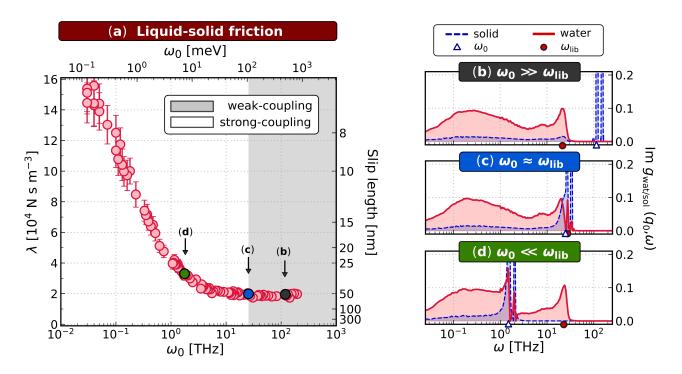Overall, our model describes two fluctuating charge

Figure 2. **Friction increases as dielectric fluctuations begin to overlap.** (a) The liquid–solid friction coefficient λ is shown against ω_0. The slip length is given as $b = \eta/\lambda$ where η is the viscosity of water. Statistical errors are obtained from block-averaging. Two regimes are indicated: weak-coupling (shaded gray) where λ remains roughly constant; and strong-coupling (not shaded) where λ increases with decreasing ω_0. In (b-d), $g_{\mathrm{wat}}(q_0, \omega)$ and $g_{\mathrm{sol}}(q_0, \omega)$ are shown for three representative cases $\omega_0 \gg \omega_{\mathrm{lib}}$, $\omega_0 \approx \omega_{\mathrm{lib}}$ and $\omega_0 \ll \omega_{\mathrm{lib}}$, respectively. We see that the increase in λ coincides with $\omega_0 \lesssim \omega_{\mathrm{lib}} \approx 20\,\mathrm{THz}$. In addition, when the overlap between the spectra is significant, the dominant features of $g_{\mathrm{sol}}(q_0, \omega)$ are broadened, and $g_{\mathrm{wat}}(q_0, \omega)$ is perturbed. The boundary between the regimes is approximate.

densities, $n_{\mathrm{wat}}(\boldsymbol{r}, t)$ of the water and $n_{\mathrm{sol}}(\boldsymbol{r}, t)$ of the solid, originating from the collective motion of water molecules and Drude oscillators, respectively, at position $\boldsymbol{r}$ and time t. The total charges of both the water and the solid are strictly conserved. It will be convenient to characterize these charge distributions by their surface response functions,[34,59] e.g., for water,

$$
\operatorname{Im} g_{\mathrm{wat}}(q, \omega) = \frac{\pi \omega}{q \mathcal{A} k_{\mathrm{B}} T} \int_{-\infty}^{\infty} \mathrm{d}t\, \mathrm{e}^{i\omega t}
$$
$$
\sum_{\alpha, \beta \in \mathrm{wat}} \left\langle Q_\alpha Q_\beta\, \mathrm{e}^{-i\boldsymbol{q}\cdot[\boldsymbol{x}_\alpha(t) - \boldsymbol{x}_\beta(0)]} \mathrm{e}^{-q|\Delta z_\alpha(t)|}\, \mathrm{e}^{-q|\Delta z_\beta(0)|} \right\rangle,
$$
$$
(1)
$$

where $\mathcal{A}$ is the interfacial lateral area, k_{B} is Boltzmann's constant, T is the temperature, $\boldsymbol{q}$ is a wavevector parallel to the surface and Q_α is the charge on atom α whose position in the plane of the graphene sheet at time t is $\boldsymbol{x}_\alpha(t)$ with vertical coordinate $z_\alpha(t) = z_0 + \Delta z_\alpha(t)$, where z_0 defines a plane between the carbon atoms and the water contact layer. The surface response function of the solid, $g_{\mathrm{sol}}(q, \omega)$, is similarly defined.

In Fig. 1(c), we present $g_{\mathrm{sol}}(q_0, \omega)$ for $m_{\mathrm{D}} = 10^3\,\mathrm{u}$ both in the absence and presence of water, where $q_0 = 2\pi/L_x \approx 0.25\,\text{Å}^{-1}$ corresponds to a low wavevector accessible in the simulation box. In the absence of water,

$g_{\mathrm{sol}}(q_0, \omega)$ exhibits two dominant peaks (see SI). We will focus on the lower frequency peak, whose position we take to be ω_0. As $\omega_0 \approx \omega_{\mathrm{D}}$, it is appropriate to consider the graphene sheet as a set of weakly coupled harmonic oscillators (see SI). In the presence of water, both of these peaks are broadened, and we also see the emergence of a broad feature at low frequencies. We will discuss the implication of these observations in the context of friction below. Further technical details of the model, simulation setup, precise definitions of computed quantities and additional tests for the sensitivity of our results to the choice of simulation settings are given in the SI.

Friction at the water–carbon interface depends sensitively on ω_0. We proceed to explore how the features of $g_{\mathrm{sol}}(q_0, \omega)$ affect friction at the interface. For each value of m_{D}, we perform equilibrium MD simulations to extract the liquid–solid friction coefficient λ from the well-established Green–Kubo relationship:[32,60]

$$
\lambda = \frac{1}{\mathcal{A} k_{\mathrm{B}} T} \int_0^\infty \mathrm{d}\tau\, \langle \mathcal{F}(0)\, \mathcal{F}(\tau) \rangle, \tag{2}
$$

where $\mathcal{F}(\tau)$ is the total force acting on the liquid along a cartesian direction lateral to the graphene sheet at time τ and $\langle \cdots \rangle$ indicates an ensemble average.

In Fig. 2(a), we show the dependence of λ on ω_0 in the range $10^{-2} - 10^2\,\mathrm{THz}$ from a total of 97 simula-

tions. Overall, as ω_0 decreases, λ stays constant until $\omega_0 \approx \omega_{\text{lib}} \approx 20\,\text{THz}$, whereupon further decreasing ω_0 leads to a significant increase in λ. To rationalize this observation, we inspect $g_{\text{wat}}(q_0, \omega)$ and $g_{\text{sol}}(q_0, \omega)$, as shown in Figs. 2(b–d), for three representative cases. Based on the relative positions of ω_0 (the principal frequency of the solid) and ω_{lib} (liquid water's librational frequency), we separate the liquid–solid frictional response into two regimes:

(i) Weak-coupling regime: When $\omega_0 \gtrsim \omega_{\text{lib}}$, the friction coefficient remains roughly constant at $\lambda \approx 1.9 \times 10^4\,\text{N s m}^{-3}$. This value agrees well with previous simulations of water on graphitic surfaces.[27,31,61–64] In this regime, there is a large separation of timescales between the dielectric modes of water and the substrate. As a result, there is little overlap between $g_{\text{sol}}(q_0, \omega)$ and $g_{\text{wat}}(q_0, \omega)$, as seen in Fig. 2(b), and water's dynamics are largely unaffected by varying ω_0. The motions of the Drude oscillators and the water are not strongly coupled.

(ii) Strong-coupling regime: When $\omega_0 \lesssim \omega_{\text{lib}}$, hydrodynamic friction increases as ω_0 decreases, reaching $\lambda \approx 15 \times 10^4\,\text{N s m}^{-3}$ for $\omega_0 \approx 0.03\,\text{THz}$. This change in friction of just over one order of magnitude would lead to a significant change in the corresponding slip length from $\sim 60\,\text{nm}$ to $\sim 7\,\text{nm}$. For comparison, experiments have reported water slippage in the range of $0 - 200$ nm on graphene[24] and $8 - 13$ nm on graphite.[21–23] In this regime, there is no longer a large separation in timescales between the Drude oscillators and water's dielectric modes. Consequently, as seen in Figs. 2(c) and (d), $g_{\text{sol}}(q_0, \omega)$ now overlaps strongly with water's librational and Debye modes, causing changes in $g_{\text{wat}}(q_0, \omega)$ that reflect the dominant features of $g_{\text{sol}}(q_0, \omega)$. The onset of this regime is further supported by the broadening of the dominant peaks in $g_{\text{sol}}(q_0, \omega)$ and changes in the spectrum of the lateral force on the liquid (see SI). We conclude that the increase in friction in this strong-coupling regime is indeed due to coupling of the dielectric modes in the water and the substrate.

To test the sensitivity of this separation into strong- and weak-coupling regimes to the details of the system, we have also performed simulations with different harmonic potentials for the Drude oscillators and a flexible water model (see SI). While differences in the absolute values of λ are expected, and indeed observed, the increase of λ for $\omega_0 \lesssim \omega_{\text{lib}}$ is robust.

Comparing molecular simulations with quantum friction theory. Before further analysis, it is useful to make a comparison of our simulation results to QF theory.[34] Kavokine *et al.* separated the liquid–solid friction into $\lambda = \lambda_{\text{SR}} + \lambda_{\text{Q}}$, where λ_{SR} is the classical surface roughness contribution and

$$\lambda_{\text{Q}} = \frac{\hbar^2}{8\pi^2 k_{\text{B}} T} \int_0^\infty \mathrm{d}q\, q^3$$
$$\int_0^\infty \frac{\mathrm{d}\omega}{\sinh^2(\hbar\omega/2k_{\text{B}}T)} \frac{\operatorname{Im} g_{\text{sol}}(q,\omega) \operatorname{Im} g_{\text{wat}}(q,\omega)}{|1 - g_{\text{sol}}(q,\omega)\, g_{\text{wat}}(q,\omega)|^2} \quad (3)$$

is the contribution from quantum friction. In our simulations, changing m_{D} does not affect static equilibrium properties such as surface roughness (see SI). In analogy to QF, then, we also decompose the friction coefficient from simulation as $\lambda(\omega_0) = \lambda_{\text{SR}} + \lambda_{\text{THz}}(\omega_0)$, where λ_{THz} originates from the coupling of charge density fluctuations in the THz regime.[65] We can obtain approximate expressions for $g_{\text{sol}}(q,\omega)$ and $g_{\text{wat}}(q,\omega)$ appropriate for our simulations. As detailed in the SI, for $g_{\text{wat}}(q,\omega)$ we use a parameterization specified in Ref. 34 for SPC/E in contact with graphene/graphite. For $g_{\text{sol}}(q,\omega)$, we parameterize a semiclassical Drude model for the surface plasmon[66] to roughly capture the intensity and width of the principal peak of $g_{\text{sol}}(q,\omega)$ observed in our simulations. In Fig. 3(a), we compare λ_{Q} given by Eq. 3 using these suitably parameterized surface response functions to λ_{THz} obtained directly from our simulations. The excellent agreement between the simulation result and Eq. 3 provides strong support for the theory of quantum friction outlined in Ref. 34.

The microscopic signatures of quantum friction manifest in the solid, not the liquid. A major advantage of performing molecular simulations is the insight they can provide at the microscopic scale. While treating electronic motion as a set of weakly coupled classical Drude oscillators lacks any explicit treatment of quantum mechanical effects, the good agreement between this classical model and QF reinforces the importance of water's low-frequency dielectric modes in any potential nonadiabatic contributions to friction at water–carbon interfaces.

Going further, we follow Ref. 62 by disentangling the origin of the friction at the interface by reformulating Eq. 2 as $\lambda = \langle \mathcal{F}^2 \rangle \tau_{\text{F}} / (\mathcal{A} k_{\text{B}} T)$, such that the mean-squared force $\langle \mathcal{F}^2 \rangle$ and force decorrelation time τ_{F} quantify static and dynamical components, respectively. As seen in Fig. 3(b), the static component remains essentially constant across the entire range of ω_0 explored. This implies that the water molecules experience the same free energy surface at the interface, an example of which is shown in Fig. 3(b, inset), independent of ω_0 (see SI). This confirms that the physical origins of λ_{THz} are not captured by the corrugation of the free energy surface that has been widely used to account for the curvature dependence of friction in CNTs[27,31] and certain differences in hydrodynamic slippage at different materials.[31,33,61,62,67] Instead, the nature of λ_{THz} is entirely dynamical, with the dependence of τ_{F} on ω_0 accounting entirely for the increase in λ_{THz}, as seen in Fig. 3(c).

The above analysis demonstrates that microscopic signatures of nonadiabatic friction should manifest in dynamical rather than static properties of the system. We
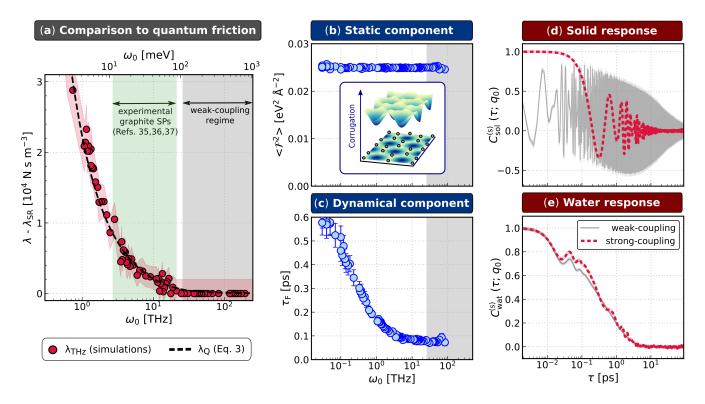
Figure 3. **Microscopic signatures of quantum friction.** (a) The prediction of QF (λ_Q, Eq. 3) well describes λ_{THz} obtained directly from molecular simulations. The shaded red region indicates the standard deviation from block-averaging. A range of frequencies for experimental surface plasmons (SPs) in graphite is indicated by the green shaded region. (b) The static component of the total friction $\langle \mathcal{F}^2 \rangle$ is essentially independent of ω_0 and therefore, all liquid–solid interfaces simulated have the same free energy surface shown in the inset (see SI for more details). (c) In contrast, the dynamical component τ_F fully captures the dependence of λ on ω_0. Surface charge density correlation functions are shown for representative cases from the weak-coupling ($\omega_0 \approx 100\,\text{THz}$) and strong-coupling ($\omega_0 \approx 1\,\text{THz}$) regimes for (d) the solid and (e) water. $C_{sol}^{(s)}(\tau; q_0)$ decays much more quickly in the strong-coupling regime, while changes to $C_{wat}^{(s)}(\tau; q_0)$ are much less pronounced. The legend in panel (e) also applies to panel (d).

therefore consider the surface charge densities, e.g, for water,

$$\tilde{n}_{wat}^{(s)}(q, t) = \sum_{\alpha \in wat} Q_\alpha e^{i\boldsymbol{q} \cdot \boldsymbol{x}_\alpha(t)} e^{-q|\Delta z_\alpha(t)|},$$

and inspect their autocorrelation functions $C_{sol}^{(s)}(\tau; q)$ and $C_{wat}^{(s)}(\tau; q)$; these are presented in Figs. 3(d) and 3(e) respectively, for $q = q_0$. While small changes in $C_{wat}^{(s)}(\tau; q)$ are observed between the weak- and strong-coupling regimes, the impact on $C_{sol}^{(s)}(\tau; q)$ is much more pronounced. For the water film, we have also probed molecular reorientation and hydrogen bond relaxations, and found that these are barely affected between the two regimes. This suggests that quantum friction is unlikely to have a significant impact on water's local dynamical properties.

We attribute these contrasting behaviors of the liquid and the solid to the rigidity of water's hydrogen-bond network, which lacks a clear counterpart from the perspective of the Drude oscillators. In fact, it is even useful to simply compare the relative magnitude of the

dipoles for a single water molecule μ_{wat} and a Drude oscillator μ_D. With our simple point charge model, we have $\langle \mu_{wat} \rangle = 2.351\,\text{D}$ while $\langle \mu_D \rangle = Q_D(3k_BT/k_D)^{1/2} \approx 0.4\,\text{D}$. Thus, while the water molecules only feel the presence of the Drude oscillators as a small perturbation relative to their intermolecular interactions, the Drude oscillators feel the impact of the water molecules much more strongly. We speculate that this conclusion also applies to cases where electronic degrees of freedom have been accurately accounted for.

In summary, by using a simple model of charge density fluctuations in a carbon substrate in which we can finely tune the surface response function of the substrate, we find increases in interfacial friction in line with those suggested by a recent theory of quantum friction. We see that the friction increases once the principal peak in the substrate's surface response function overlaps with features in water's surface response function arising from its librational and Debye modes. We show that this extra contribution to the friction is entirely dynamical in its origin, with static equilibrium properties apparently indifferent to the degree of coupling between the water and

the substrate. The insights provided by our molecular simulations reveal that the increase in friction manifests at the microscopic scale as a pronounced change in the relaxation of the substrate's dielectric modes, with relatively little impact on the behavior of water.

Our model, while able to provide a proof of concept for QF, does not aim to be a rigorous description of water on graphite. We have considered a static graphene sheet, which precludes any role that phonon modes might play.[68–72] Any changes in surface roughness upon changing from single to multilayer systems have also not been accounted for. Going forwards, it will be essential to explore how these factors affect both the surface roughness and charge density coupling contributions to friction. Advances in simulations of nonadiabatic effects[43,73,74] to accurately describe the solid's electronic excitations in response to collective fluctuations in the liquid will also be a welcome development. An obvious limitation of the present model is that it is restricted to describing the substrate as a dielectric, rather than a conductor (or semimetal). In principle, extending the current methodology to classical representations of metallic substrates[75,76] should be relatively straightforward.

Despite its simplifications, our model captures the increase in the interfacial friction when there is an overlap in the dielectric spectra of the liquid and the solid. It is important to stress that this principle can be generalized to the interfaces of any combination of polar liquid and solid. Since the THz densities of state of a liquid can be reasonably described in simulations, our model opens up the possibility to predict whether different liquids[77,78] also show a significant QF component. In addition to providing early evidence from simulations in general support of QF theory, our results suggest a potentially useful strategy for experimental verification. Specifically, the apparent asymmetry between the impact on water and the substrate suggests it may be advantageous to focus experimental efforts on spectroscopies that probe the substrate's electronic response,[79] rather than seeking hallmarks in the structure or dynamics of the liquid.

ACKNOWLEDGMENTS

SUPPORTING INFORMATION

The supporting information provides additional details on the results presented in the main article. This includes: the model and simulation details; precise definitions and computational details of the quantities presented in the article; further analysis on the coupling of the liquid and solid charge densities; sensitivity of the results to certain aspects of the simulations and the model; detailed comparison to quantum friction theory and analyses on additional properties of the interface.

DATA AVAILABILITY STATEMENT

The data that support the findings of this study are openly available at the University of Cambridge Data Repository at https://doi.org/10.17863/CAM.89536.

REFERENCES

[1] L. Bocquet and E. Charlaix, "Nanofluidics, from bulk to interfaces," Chem. Soc. Rev. **39**, 1073–1095 (2010).
[2] L. Bocquet, "Nanofluidics coming of age," Nature Materials **19**, 254–256 (2020).
[3] M. A. Shannon, P. W. Bohn, M. Elimelech, J. G. Georgiadis, B. J. Mariñas, and A. M. Mayes, "Science and technology for water purification in the coming decades," Nature **452**, 301–310 (2008).
[4] M. Elimelech and W. A. Phillip, "The future of seawater desalination: Energy, technology, and the environment," Science **333**, 712–717 (2011).
[5] D. Cohen-Tanugi and J. C. Grossman, "Water desalination across nanoporous graphene," Nano Letters **12**, 3602–3608 (2012).
[6] P. Simon and Y. Gogotsi, "Materials for electrochemical capacitors," Nature Materials **7**, 845–854 (2008).
[7] L. L. Zhang and X. S. Zhao, "Carbon-based materials as supercapacitor electrodes," Chem. Soc. Rev. **38**, 2520–2531 (2009).
[8] B. E. Logan and M. Elimelech, "Membrane-based processes for sustainable power generation using water," Nature **488**, 313–319 (2012).
[9] A. Siria, P. Poncharal, A.-L. Biance, R. Fulcrand, X. Blase, S. T. Purcell, and L. Bocquet, "Giant osmotic energy conversion measured in a single transmembrane boron nitride nanotube," Nature **494**, 455–458 (2013).
[10] H. G. Park and Y. Jung, "Carbon nanofluidics of rapid water transport for energy applications," Chem. Soc. Rev. **43**, 565–576 (2014).
[11] A. Siria, M.-L. Bocquet, and L. Bocquet, "New avenues for the large-scale harvesting of blue energy," Nature Reviews Chemistry **1**, 0091 (2017).
[12] O. Björneholm, M. H. Hansen, A. Hodgson, L.-M. Liu, D. T. Limmer, A. Michaelides, P. Pedevilla, J. Rossmeisl, H. Shen, G. Tocci, E. Tyrode, M.-M. Walz, J. Werner, and H. Bluhm, "Water at interfaces," Chemical Reviews **116**, 7698–7726 (2016).
[13] S. Faucher, N. Aluru, M. Z. Bazant, D. Blankschtein, A. H. Brozena, J. Cumings, J. Pedro de Souza, M. Elimelech, R. Epsztein, J. T. Fourkas, A. G. Rajan, H. J. Kulik, A. Levy, A. Majumdar, C. Martin, M. McEldrew, R. P. Misra, A. Noy, T. A. Pham, M. Reed, E. Schwegler, Z. Siwy, Y. Wang, and M. Strano,

"Critical knowledge gaps in mass transport through single-digit nanopores: A review and perspective," The Journal of Physical Chemistry C **123**, 21309–21326 (2019).

[14] D. Muñoz-Santiburcio and D. Marx, "Confinement-controlled aqueous chemistry within nanometric slit pores," Chemical Reviews **121**, 6293–6320 (2021).

[15] A. Striolo, A. Michaelides, and L. Joly, "The carbon–water interface: Modeling challenges and opportunities for the water–energy nexus," Annual Review of Chemical and Biomolecular Engineering **7**, 533–556 (2016).

[16] J. K. Holt, H. G. Park, Y. Wang, M. Stadermann, A. B. Artyukhin, C. P. Grigoropoulos, A. Noy, and O. Bakajin, "Fast mass transport through sub-2-nanometer carbon nanotubes," Science **312**, 1034–1037 (2006).

[17] M. Whitby, L. Cagnon, M. Thanou, and N. Quirke, "Enhanced fluid flow through nanoscale carbon pipes," Nano Letters **8**, 2632–2637 (2008).

[18] X. Qin, Q. Yuan, Y. Zhao, S. Xie, and Z. Liu, "Measurement of the rate of water translocation through carbon nanotubes," Nano Letters **11**, 2173–2177 (2011).

[19] R. H. Tunuguntla, R. Y. Henley, Y.-C. Yao, T. A. Pham, M. Wanunu, and A. Noy, "Enhanced water permeability and tunable ion selectivity in subnanometer carbon nanotube porins," Science **357**, 792–796 (2017).

[20] A. Keerthi, S. Goutham, Y. You, P. Iamprasertkun, R. A. W. Dryfe, A. K. Geim, and B. Radha, "Water friction in nanofluidic channels made from two-dimensional crystals," Nature Communications **12**, 3092 (2021).

[21] A. Maali, T. Cohen-Bouhacina, and H. Kellay, "Measurement of the slip length of water flow on graphite surface," Applied Physics Letters **92**, 053101 (2008).

[22] D. Ortiz-Young, H.-C. Chiu, S. Kim, K. Voïtchovsky, and E. Riedo, "The interplay between apparent viscosity and wettability in nanoconfined water," Nature Communications **4**, 2482 (2013).

[23] S. Li, Q. Li, R. W. Carpick, P. Gumbsch, X. Z. Liu, X. Ding, J. Sun, and J. Li, "The evolving quality of frictional contact with graphene," Nature **539**, 541–545 (2016).

[24] Q. Xie, M. A. Alibakhshi, S. Jiao, Z. Xu, M. Hempel, J. Kong, H. G. Park, and C. Duan, "Fast water transport in graphene nanofluidic channels," Nature Nanotechnology **13**, 238–245 (2018).

[25] M. Majumder, N. Chopra, R. Andrews, and B. J. Hinds, "Enhanced flow in carbon nanotubes," Nature **438**, 44–44 (2005).

[26] E. Secchi, S. Marbach, A. Niguès, D. Stein, A. Siria, and L. Bocquet, "Massive radius-dependent flow slippage in carbon nanotubes," Nature **537**, 210–213 (2016).

[27] K. Falk, F. Sedlmeier, L. Joly, R. R. Netz, and L. Bocquet, "Molecular origin of fast water transport in carbon nanotube membranes: Superlubricity versus curvature dependent friction," Nano Letters **10**, 4067–4073 (2010).

[28] J. A. Thomas and A. J. H. McGaughey, "Reassessing fast water transport through carbon nanotubes," Nano Letters **8**, 2788–2793 (2008).

[29] F. Leoni, C. Calero, and G. Franzese, "Nanoconfined fluids: Uniqueness of water compared to other liquids," ACS Nano **15**, 19864–19876 (2021).

[30] G. Cicero, J. C. Grossman, E. Schwegler, F. Gygi, and G. Galli, "Water confined in nanotubes and between graphene sheets: A first principle study," Journal of the American Chemical Society **130**, 1871–1878 (2008).

[31] F. L. Thiemann, C. Schran, P. Rowe, E. A. Müller, and A. Michaelides, "Water flow in single-wall nanotubes: Oxygen makes it slip, hydrogen makes it stick," ACS Nano **16**, 10775–10782 (2022).

[32] J.-L. Barrat and L. Bocquet, "Influence of wetting properties on hydrodynamic boundary conditions at a fluid/solid interface," Faraday Discuss. **112**, 119–128 (1999).

[33] K. Falk, F. Sedlmeier, L. Joly, R. R. Netz, and L. Bocquet, "Ultralow liquid/solid friction in carbon nanotubes: Comprehensive theory for alcohols, alkanes, OMCTS, and water," Langmuir **28**, 14261–14272 (2012).

[34] N. Kavokine, M.-L. Bocquet, and L. Bocquet, "Fluctuation-induced quantum friction in nanoscale water flows," Nature **602**, 84–90 (2022).

[35] M. Portail, M. Carrere, and J. M. Layet, "Dynamical properties of graphite and peculiar behaviour of the low-energy plasmon," Surface Science **433-435**, 863–867 (1999).

[36] E. T. Jensen, R. E. Palmer, W. Allison, and J. F. Annett, "Temperature-dependent plasmon frequency and linewidth in a semimetal," Phys. Rev. Lett. **66**, 492–495 (1991).

[37] Q. Xing, C. Song, C. Wang, Y. Xie, S. Huang, F. Wang, Y. Lei, X. Yuan, C. Zhang, L. Mu, Y. Huang, F. Xiu, and H. Yan, "Tunable terahertz plasmons in graphite thin films," Phys. Rev. Lett. **126**, 147401 (2021).

[38] G. E. Walrafen, "Raman spectrum of water: transverse and longitudinal acoustic modes below 300 cm^{-1} and optic modes above 300 cm^{-1}," The Journal of Physical Chemistry **94**, 2237–2239 (1990).

[39] I. Ohmine and S. Saito, "Water dynamics: Fluctuation, relaxation, and chemical reactions in hydrogen bond network rearrangement," Accounts of Chemical Research **32**, 741–749 (1999).

[40] M. Heyden, J. Sun, S. Funkner, G. Mathias, H. Forbert, M. Havenith, and D. Marx, "Dissecting the THz spectrum of liquid water from first principles via correlations in time and space," Proceedings of the National Academy of Sciences **107**, 12068–12073 (2010).

[41] M. Born and R. Oppenheimer, "Zur quantentheorie der molekeln," Annalen der Physik **389**, 457–484 (1927).

[42] W. Dou and J. E. Subotnik, "Perspective: How to understand electronic friction," The Journal of Chemical Physics **148**, 230901 (2018).

[43] M. Head-Gordon and J. C. Tully, "Molecular dynamics with electronic frictions," The Journal of Chemical Physics **103**, 10137–10145 (1995).

[44] R. Martinazzo and I. Burghardt, "Quantum dynamics with electronic friction," Phys. Rev. Lett. **128**, 206002 (2022).

[45] M. Askerka, R. J. Maurer, V. S. Batista, and J. C. Tully, "Role of tensorial electronic friction in energy transfer at metal surfaces," Phys. Rev. Lett. **116**, 217601 (2016).

[46] R. Yin, Y. Zhang, and B. Jiang, "Strong vibrational relaxation of NO scattered from Au(111): Importance of the adiabatic potential energy surface," The Journal of Physical Chemistry Letters **10**, 5969–5974 (2019).

[47] G. Füchsel, X. Zhou, B. Jiang, J. I. Juaristi, M. Alducin, H. Guo, and G.-J. Kroes, "Reactive and nonreactive scattering of HCl from Au(111): An ab initio molecular dynamics study," The Journal of Physical Chemistry C **123**, 2287–2299 (2019).

[48] Y. Litman, E. S. Pós, C. L. Box, R. Martinazzo, R. J. Maurer, and M. Rossi, "Dissipative tunneling rates through the incorporation of first-principles electronic friction in instanton rate theory. ii. benchmarks and applications," The Journal of Chemical Physics **156**, 194107 (2022).

[49] B. Hellsing and M. Persson, "Electronic damping of atomic and molecular vibrations at metal surfaces," Physica Scripta **29**, 360–371 (1984).

[50] J. I. Juaristi, M. Alducin, R. D. Muiño, H. F. Busnengo, and A. Salin, "Role of electron-hole pair excitations in the dissociative adsorption of diatomic molecules on metal surfaces," Phys. Rev. Lett. **100**, 116102 (2008).

[51] P. Zarzycki and B. Gilbert, "Temperature-dependence of the dielectric relaxation of water using non-polarizable water models," Physical Chemistry Chemical Physics **22**, 1011–1018 (2020).

[52] S. Carlson, F. N. Brünig, P. Loche, D. J. Bonthuis, and R. R. Netz, "Exploring the absorption spectrum of simulated water from MHz to infrared," The Journal of Physical Chemistry A **124**, 5599–5605 (2020).

[53] H. J. C. Berendsen, J. R. Grigera, and T. P. Straatsma, "The missing term in effective pair potentials," The Journal of Physical Chemistry **91**, 6269–6271 (1987).

[54] T. Werder, J. H. Walther, R. L. Jaffe, T. Halicioglu, and P. Koumoutsakos, "On the water–carbon interaction for use in molecular dynamics simulations of graphite and carbon nanotubes," The Journal of Physical Chemistry B **107**, 1345–1352 (2003).

[55] G. Lamoureux and B. Roux, "Modeling induced polarization with classical Drude oscillators: Theory and molecular dynamics simulation algorithm," The Journal of Chemical Physics **119**, 3025–3039 (2003).

[56] R. P. Misra and D. Blankschtein, "Insights on the role of many-body polarization effects in the wetting of graphitic surfaces by water," The Journal of Physical Chemistry C **121**, 28166–28179 (2017).

[57] R. Car and M. Parrinello, "Unified approach for molecular dynamics and density-functional theory," Phys. Rev. Lett. **55**, 2471–2474 (1985).

[58] M. Sprik, "Computer simulation of the dynamics of induced polarization fluctuations in water," The Journal of Physical Chemistry **95**, 2283–2291 (1991).

[59] J. M. Pitarke, V. M. Silkin, E. V. Chulkov, and P. M. Echenique, "Theory of surface plasmons and surface-plasmon polaritons," Reports on Progress in Physics **70**, 1–87 (2006).

[60] L. Bocquet and J.-L. Barrat, "On the Green–Kubo relationship for the liquid-solid friction coefficient," The Journal of Chemical Physics **139**, 044704 (2013).

[61] G. Tocci, L. Joly, and A. Michaelides, "Friction of water on graphene and hexagonal boron nitride from ab initio methods: Very different slippage despite very similar interface structures," Nano Letters **14**, 6872–6877 (2014).

[62] G. Tocci, M. Bilichenko, L. Joly, and M. Iannuzzi, "Ab initio nanofluidics: disentangling the role of the energy landscape and of density correlations on liquid/solid friction," Nanoscale **12**, 10994–11000 (2020).

[63] A. Govind Rajan, M. S. Strano, and D. Blankschtein, "Liquids with lower wettability can exhibit higher friction on hexagonal boron nitride: The intriguing role of solid–liquid electrostatic interactions," Nano Letters **19**, 1539–1551 (2019).

[64] A. R. Poggioli and D. T. Limmer, "Distinct chemistries explain decoupling of slip and wettability in atomically smooth aqueous interfaces," The Journal of Physical Chemistry Letters **12**, 9060–9067 (2021).

[65] In practice, we obtain λ_{SR} as the average value of λ in the weak-coupling regime and then obtain λ_{THz} by subtraction.

[66] S. Pisana, M. Lazzeri, C. Casiraghi, K. S. Novoselov, A. K. Geim, A. C. Ferrari, and F. Mauri, "Breakdown of the adiabatic Born–Oppenheimer approximation in graphene," Nature Materials **6**, 198–201 (2007).

[67] T. A. Ho, D. V. Papavassiliou, L. L. Lee, and A. Striolo, "Liquid water can slip on a hydrophilic surface," Proceedings of the National Academy of Sciences **108**, 16170–16175 (2011).

[68] M. Ma, F. Grey, L. Shen, M. Urbakh, S. Wu, J. Z. Liu, Y. Liu, and Q. Zheng, "Water transport inside carbon nanotubes mediated by phonon-induced oscillating friction," Nature Nanotechnology **10**, 692–695 (2015).

[69] L. Bocquet and R. R. Netz, "Phonon modes for faster flow," Nature Nanotechnology **10**, 657–658 (2015).

[70] E. R. Cruz-Chú, E. Papadopoulou, J. H. Walther, A. Popadić, G. Li, M. Praprotnik, and P. Koumoutsakos, "On phonons and water flow enhancement in carbon nanotubes," Nature Nanotechnology **12**, 1106–1108 (2017).

[71] S. Marbach, D. S. Dean, and L. Bocquet, "Transport and dispersion across wiggling nanopores," Nature Physics **14**, 1108–1113 (2018).

[72] A. Ambrosetti, G. Palermo, and P. L. Silvestrelli, "Quantum-mechanically enhanced water flow in subnanometer carbon nanotubes," The Journal of Physical Chemistry C **126**, 20174–20182 (2022).

[73] G. Mazzola, A. Zen, and S. Sorella, "Finite-temperature electronic simulations without the born-oppenheimer constraint," The Journal of Chemical Physics **137**, 134112 (2012).

[74] N. M. Tubman, I. Kylänpää, S. Hammes-Schiffer, and D. M. Ceperley, "Beyond the born-oppenheimer approximation with quantum monte carlo methods," Phys. Rev. A **90**, 042507 (2014).

[75] A. Coretti, C. Bacon, R. Berthin, A. Serva, L. Scalfi, I. Chubak, K. Goloviznina, M. Haefele, A. Marin-Laflèche, B. Rotenberg, S. Bonella, and M. Salanne, "Metalwalls: Simulating electrochemical interfaces between polarizable electrolytes and metallic electrodes," The Journal of Chemical Physics **157**, 184801 (2022).

[76] J. I. Siepmann and M. Sprik, "Influence of surface topology and electrostatic potential on water/electrode systems," The Journal of Chemical Physics **102**, 511–524 (1995).

[77] P.-A. Cazade, R. Hartkamp, and B. Coasne, "Structure and dynamics of an electrolyte confined in charged nanopores," The Journal of Physical Chemistry C **118**, 5061–5072 (2014).

[78] R. Futamura, T. Iiyama, Y. Takasaki, Y. Gogotsi, M. J. Biggs, M. Salanne, J. Ségalini, P. Simon, and K. Kaneko, "Partial breaking of the coulombic ordering of ionic liquids confined in carbon nanopores," Nature Materials **16**, 1225–1232 (2017).

[79] R. Ulbricht, E. Hendry, J. Shan, T. F. Heinz, and M. Bonn, "Carrier dynamics in semiconductors studied with time-resolved terahertz spectroscopy," Rev. Mod. Phys. **83**, 543–586 (2011).

Supporting Information for: Classical Quantum Friction at Water–Carbon Interfaces

Anna T. Bui,[1] Fabian L. Thiemann,[2,1,3] Angelos Michaelides,[1] and Stephen J. Cox[1]

[1] *Yusuf Hamied Department of Chemistry, University of Cambridge, Lensfield Road, Cambridge, CB2 1EW, United Kingdom*

[2] *Thomas Young Centre, London Centre for Nanotechnology, and Department of Physics and Astronomy, University College London, Gower Street, London, WC1E 6BT, United Kingdom*

[3] *Department of Chemical Engineering, Sargent Centre for Process Systems Engineering, Imperial College London, South Kensington Campus, London, SW7 2AZ, United Kingdom*

(Dated: January 10, 2023)

This supplementary information provides additional details on the results presented in the main article. This includes: the model and simulation details; precise definitions and computational details of the quantities presented in the article; further analysis on the coupling of the liquid and solid charge densities; sensitivity of the results to certain aspects of the simulations and the model; comparison to quantum friction theory and analyses on additional properties of the interface.

CONTENTS

S1. CLASSICAL MOLECULAR DYNAMICS SIMULATION DETAILS

S1.1. Model description

We consider a system of a film of liquid water on a flat graphene sheet as described in the main article. Liquid water can be modeled by rigid simple point charge models with potential energy functions of the form

$$\mathcal{U}_{\text{wat}}(\boldsymbol{R}_{\text{wat}}^N) = \sum_{i<j}^N u_{\text{LJ}}(|\boldsymbol{r}_{\text{O},i} - \boldsymbol{r}_{\text{O},j}|) + \sum_{i<j}^N \sum_{\alpha,\beta} \frac{Q_{\alpha,i}Q_{\beta,j}}{|\boldsymbol{r}_{\alpha,i} - \boldsymbol{r}_{\beta,j}|}, \tag{S1}$$

where $\boldsymbol{R}_{\text{wat}}^N$ denotes the set of atomic positions for a configuration of N water molecules, $\boldsymbol{r}_{\text{O},i}$ denotes position of the oxygen atom on water molecule i and $Q_{\alpha,i}$ is the charge of site α located at position $\boldsymbol{r}_{\alpha,i}$. The first set of sums in Eq. S1 captures short-ranged repulsion and non-electrostatic "long-ranged" attraction between water molecules with the usual Lennard-Jones 12-6 potential

$$u_{\text{LJ}}(r) = 4\epsilon \left[\left(\frac{\sigma}{r}\right)^{12} - \left(\frac{\sigma}{r}\right)^6 \right], \tag{S2}$$

which is parameterized by an energy scale ϵ and a length scale σ. The second set of sums in Eq. S1 describes electrostatic interactions. Here, we adopt a unit system for electrostatics in which $4\pi\epsilon_0 = 1$ where ϵ_0 is the permittivity of free space.

In the standard surface roughness picture, the liquid interacts with the solid through long-ranged van der Waals attraction and short-range Pauli repulsion, which we model with a 12-6 Lennard-Jones potential between the oxygen atoms on the water and the carbon atoms in the graphene sheet

$$\mathcal{U}_{\text{SR}}(\boldsymbol{R}_{\text{wat}}^N, \boldsymbol{R}_{\text{sol}}^M) = \sum_i^N \sum_j^M u_{\text{LJ}}(|\boldsymbol{r}_{\text{O},i} - \boldsymbol{r}_{\text{C},j}|), \tag{S3}$$

where $\boldsymbol{R}_{\text{sol}}^M$ denotes the set of atomic positions for a configuration of M carbon atoms. Here, for simplicity, we fix the positions of the carbon atoms.

Polarization of the solid can then be incorporated with the classical Drude oscillator model.[1] Each carbon core now carries a positive charge $+Q_{\text{D}}$ and is attached to a Drude particle of charge $-Q_{\text{D}}$ and mass m_{D} through a harmonic spring with force constant k_{D}. The potential energy function of the solid then has the form

$$\mathcal{U}_{\text{sol}}(\boldsymbol{R}_{\text{sol}}^M) = \sum_i^M \frac{1}{2} k_{\text{D}} |\boldsymbol{r}_{\text{C},i} - \boldsymbol{r}_{\text{D},i}|^2 + \sum_{i<j}^M \sum_{\alpha,\beta} \frac{Q_{\alpha,i}Q_{\beta,j}}{|\boldsymbol{r}_{\alpha,i} - \boldsymbol{r}_{\beta,j}|} \phi(|\boldsymbol{r}_{\alpha,i} - \boldsymbol{r}_{\beta,j}|). \tag{S4}$$

The first set of sums describes the total harmonic interaction of all Drude oscillators in the solid. The second set of sums describes the electrostatic interactions between the oscillators. To avoid the "polarization catastrophe", a Thole function,[2] $\phi(r)$, is used to damp Coulomb interactions at short distances. This function has the form

$$\phi(r) = 1 - \left(1 + \frac{sr}{2}\right) e^{-sr}, \tag{S5}$$

where the scaling coefficient s is determined by the polarizability of the carbon atom α_{C} and a Thole damping parameter δ_{C} via $s = \delta_{\text{C}}/(\alpha_{\text{C}})^{1/3}$.

In the absence of a field, each Drude particle oscillates around its core atom position $\boldsymbol{r}_{\text{C}}$. In an electric field $\boldsymbol{E}(t)$, here arising from the fluctuating charge density of water, the Drude particle oscillates around $\boldsymbol{r}_{\text{C}} + \boldsymbol{d}(t)$ where $\boldsymbol{d}(t)$ is the displacement of Drude particle from the core atom at time t and is given by $\boldsymbol{d}(t) = Q_{\text{D}}\boldsymbol{E}(t)/k_{\text{D}}$. The instantaneous induced dipole from the Drude oscillator is $\boldsymbol{\mu}_{\text{D}}(t) = Q_{\text{D}}\boldsymbol{d}(t) = Q_{\text{D}}^2\boldsymbol{E}(t)/k_{\text{D}}$. The isotropic atomic polarizability is then seen to be[1,3–5]

$$\alpha_{\text{C}} = \frac{Q_{\text{D}}^2}{k_{\text{D}}}. \tag{S6}$$

The polarization response of the solid is therefore controlled by the parameters Q_D and k_D.

Introduction of point charges in the solid now introduces electrostatic interactions between the solid and the liquid, which we refer to as the charge density coupling term:

$$\mathcal{U}_{\mathrm{CC}}(\boldsymbol{R}_{\mathrm{wat}}^N, \boldsymbol{R}_{\mathrm{sol}}^M) = \sum_i^N \sum_j^M \sum_{\alpha,\beta} \frac{Q_{\alpha,i} Q_{\beta,j}}{|\boldsymbol{r}_{\alpha,i} - \boldsymbol{r}_{\beta,j}|}. \tag{S7}$$

The overall potential energy of the system is:

$$\mathcal{U}_{\mathrm{tot}}(\boldsymbol{R}_{\mathrm{wat}}^N, \boldsymbol{R}_{\mathrm{sol}}^M) = \mathcal{U}_{\mathrm{wat}}(\boldsymbol{R}_{\mathrm{wat}}^N) + \mathcal{U}_{\mathrm{SR}}(\boldsymbol{R}_{\mathrm{wat}}^N, \boldsymbol{R}_{\mathrm{sol}}^M) + \mathcal{U}_{\mathrm{sol}}(\boldsymbol{R}_{\mathrm{sol}}^M) + \mathcal{U}_{\mathrm{CC}}(\boldsymbol{R}_{\mathrm{wat}}^N, \boldsymbol{R}_{\mathrm{sol}}^M). \tag{S8}$$

We reiterate that in previous work,[6,7] classical treatments of liquid–solid interfacial friction have focused on the first two terms of the potential. Here, our model considers also interactions between fluctuating charge densities in the liquid and the solid through the addition of the last two terms.
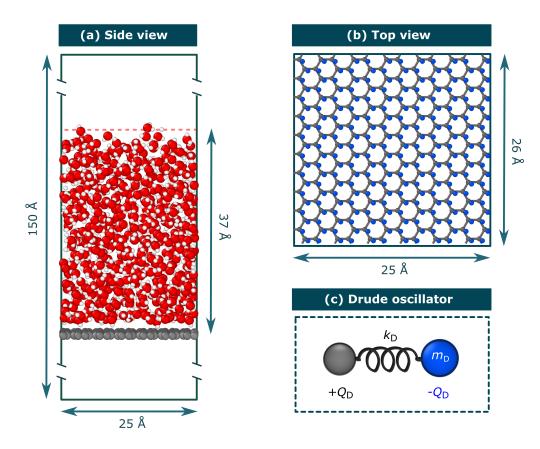
S1.2. System set-up

Figure S1. **System set-up.** The view from (a) the side of the liquid–solid interface and (b) the top of the solid sheet. Oxygen, hydrogen, carbon atoms and Drude particles are in red, white, grey and blue, respectively. The dark solid lines represent the edges of the simulation box. (c) The classical Drude oscillator is used to model charge density in the solid, whose parameters include: the harmonic spring constant k_D, the Drude mass m_D, charge on the core carbon atom $+Q_D$ and on the Drude particle $-Q_D$.

For the results presented in the main article, the simulations were carried out with 724 water molecules in a thin film of thickness $\approx 37\,\text{Å}$ above a graphene layer of 240 carbon atoms, as illustrated in Fig. S1. Each carbon atom is attached to one Drude particle so there are 240 Drude particles. The orthorhombic cell has dimension $\approx 26 \times 25 \times 150\,\text{Å}^3$. In addition, simulations of larger system sizes and of water films

with different thicknesses were also performed to check the sensitivity of the results, which are presented in Sec. S3.

S1.3. Simulation details

All simulations were carried out with the `LAMMPS` simulations package.[8,9] Water–water interactions were described with the SPC/E water model.[10] The geometry of water molecules was constrained using the `RATTLE` algorithm.[11] The carbon positions of the sheet were fixed. Water–carbon interaction responsible for the surface roughness was modeled with Werder parameters.[12] Charge densities on the graphene sheet were modeled using the classical Drude oscillator model[1,13] with Thole damping[2] using parameters from Misra and Blankschtein.[14] The value of parameters for all interaction potentials in the simulations are summarized in Tabs. S1 and S2. All Lennard-Jones interactions were truncated and shifted at 10 Å. Electrostatic interactions were cut off at 10 Å and long-ranged interactions were evaluated using particle–particle particle–mesh Ewald summation[15] such that the RMS error in the forces was a factor of 10^5 smaller than the force between two unit charges separated by a distance of 1.0 Å.[16] Drude mass choices to change the solid charge density frequency are in the range of $1 - 10^7$ amu.

Subsystem	Atom type	Mass [amu]	Charge [e]
water	O	15.9994	−0.8476
	H	1.008	+0.4238
carbon	C	*	+1.8520
	D	$1 - 10^7$	−1.8520

Table S1. **Parameters for masses and charges for atoms in simulations.** Parameters for water are from the SPC/E model[10] and those for the carbon solid are from Misra and Blankschtein.[14] The * denotes that C atoms are fixed so their masses do not contribute to the dynamics. The letter D is used to denote Drude particles.

Interaction potential	Potential form	Parameters
SPC/E[10]	rigid bond	$r_{OH} = 1.0$ Å
	rigid angle	$\theta_{HOH} = 109.47°$
	Lennard-Jones	$\epsilon_{OO} = 0.1553 \,\mathrm{kcal\,mol^{-1}}$
		$\sigma_{OO} = 3.166$ Å
Werder[12]	Lennard-Jones	$\epsilon_{CO} = 0.1553 \,\mathrm{kcal\,mol^{-1}}$
		$\sigma_{CO} = 3.190$ Å
Misra and Blankschtein[14]	Thole damping[2]	$\delta_C = 1.507$
	harmonic bond	$k_D = 1000 \,\mathrm{kcal\,mol^{-1}\,Å^{-2}}$

Table S2. **Parameters for interaction potentials (force fields) employed in simulations.** For polarization in the solid, the choice of k_D and Q_D from Misra and Blankschtein[14] gives an isotropic polarizability of $\alpha_C = 1.139$ Å^3.

The simulations were carried out in the canonical (NVT) ensemble, where the temperature was held at 300 K. Two separate Nosé–Hoover thermostats[17,18] were applied to the water and Drude particles. Each thermostat is a Nosé–Hoover chain with 10 thermostats and a damping constant of 0.1 ps. Dynamics were propagated using the velocity Verlet algorithm with a time-step of 1 fs, unless specified otherwise. Each system was equilibrated for 100 ps and the subsequent 10 ns was used for analysis to give the results presented in the main article. The sensitivity of the results to different simulation settings is presented in Sec. S3.

S2. COMPUTATION OF PROPERTIES

S2.1. Friction coefficient

For each equilibrium MD simulation, the friction coefficient was evaluated through the Green–Kubo formula[19] involving the time integral of the force autocorrelation function defined as:

$$\lambda_{\mathrm{GK}}(\tau) = \frac{1}{\mathcal{A}k_{\mathrm{B}}T} \int_0^\tau \mathrm{d}t \, \langle \mathcal{F}(0) \cdot \mathcal{F}(t) \rangle, \tag{S9}$$

where $\mathcal{A}$ is the interfacial lateral area, $\langle \cdots \rangle$ indicates an ensemble average and $\mathcal{F}(t)$ denotes the instantaneous lateral force exerted on the liquid by the solid at time t. $\mathcal{F}(t)$ is evaluated as the total summed force acting on all water molecules of a given configuration averaged over both in-plane dimensions (x, y) and is saved at every time-step (1 fs). In principle, the friction coefficient of the system is recovered at the long-time limit:

$$\lambda = \lim_{\tau \to \infty} \lambda_{\mathrm{GK}}(\tau). \tag{S10}$$

However, at long times, the integral in Eq. S9 decays to zero due to the finite lateral extent of the system[20,21] so evaluating $\lambda_{\mathrm{GK}}(\tau)$ to a plateau is commonly employed.[7,22,23] It has been shown that taking the maximum of $\lambda_{\mathrm{GK}}(\tau)$ only recovers friction correctly when there is a separation of timescales between the decay time and the memory time of the force autocorrelation function.[24] Since we are probing behaviors of the interface where there is no separation of timescales, we approximate λ as the plateaued friction coefficient averaged between correlation time of $5 - 10$ ps. Justification of this choice is detailed in Sec. S3. For each Drude mass, we perform equilibrium MD simulations to extract λ. The error bars correspond to the statistical errors obtained from splitting the entire trajectory into 100 blocks such that each block is 100 ps long.

In the main text, we decompose the static and dynamical components of the friction coefficient by reformulating the Green–Kubo expression in terms of the mean square force $\langle \mathcal{F}^2 \rangle$ and the force decorrelation time τ_{F}:

$$\lambda = \frac{1}{\mathcal{A}k_{\mathrm{B}}T} \langle \mathcal{F}^2 \rangle \tau_{\mathrm{F}}, \tag{S11}$$

where

$$\tau_{\mathrm{F}} = \int_0^\infty \mathrm{d}t \, \frac{\langle \mathcal{F}(0)\mathcal{F}(t) \rangle}{\langle \mathcal{F}^2 \rangle}. \tag{S12}$$

In practice, we computed the friction coefficient and the mean square force first before obtaining the force decorrelation time via $\tau_{\mathrm{F}} = \lambda \mathcal{A}k_{\mathrm{B}}T/\langle \mathcal{F}^2 \rangle$.

S2.2. Surface response function

In the main article, the charge density distributions of the solid and the liquid are characterized by their surface response functions defined as

$$\mathrm{Im}\, g_{\mathrm{sol}}(q, \omega) = \frac{\pi \omega}{q \mathcal{A} k_{\mathrm{B}} T} \int_{-\infty}^\infty \mathrm{d}t\, \mathrm{e}^{i\omega t} \sum_{\alpha, \beta \,\in\, \mathrm{sol}} \left\langle Q_\alpha Q_\beta \, \mathrm{e}^{-i\boldsymbol{q}\cdot[\boldsymbol{x}_\alpha(t) - \boldsymbol{x}_\beta(0)]} \mathrm{e}^{-q|z_\alpha(t) - z_0|} \, \mathrm{e}^{-q|z_\beta(0) - z_0|} \right\rangle, \tag{S13}$$

and

$$\mathrm{Im}\, g_{\mathrm{wat}}(q, \omega) = \frac{\pi \omega}{q \mathcal{A} k_{\mathrm{B}} T} \int_{-\infty}^\infty \mathrm{d}t\, \mathrm{e}^{i\omega t} \sum_{\alpha, \beta \,\in\, \mathrm{wat}} \left\langle Q_\alpha Q_\beta \, \mathrm{e}^{-i\boldsymbol{q}\cdot[\boldsymbol{x}_\alpha(t) - \boldsymbol{x}_\beta(0)]} \mathrm{e}^{-q|z_\alpha(t) - z_0|} \, \mathrm{e}^{-q|z_\beta(0) - z_0|} \right\rangle, \tag{S14}$$

respectively. Here, Q_α is the charge on atom α, whose position in the plane of the graphene sheet at time t is $\boldsymbol{x}_\alpha(t)$, $\boldsymbol{q}$ is a wavevector parallel to the graphene sheet, $z_\alpha(t)$ is the vertical coordinate and $z_0 = 1.6$ Å above the graphene sheet defines a plane between carbon atoms and the water contact layer.

In practice, we computed at every time-step $(1\,\mathrm{fs})$ the Fourier–Laplace surface components of the charge densities for the solid and the liquid, defined as

$$\tilde{n}_{\mathrm{sol}}^{(\mathrm{s})}(q,t) = \sum_{\alpha \in \mathrm{sol}} Q_\alpha e^{i\boldsymbol{q}\cdot\boldsymbol{x}_\alpha(t)} e^{-q|z_\alpha(t)-z_0|}, \tag{S15}$$

and

$$\tilde{n}_{\mathrm{wat}}^{(\mathrm{s})}(q,t) = \sum_{\alpha \in \mathrm{wat}} Q_\alpha e^{i\boldsymbol{q}\cdot\boldsymbol{x}_\alpha(t)} e^{-q|z_\alpha(t)-z_0|}, \tag{S16}$$

respectively. As we are interested in the long-wavelength limit $(q \to 0)$, we focus on $\boldsymbol{q} = \boldsymbol{q}_0$, the lowest wavevector in the x direction accessible in our simulation box, the magnitude of which is $q_0 = 2\pi/L_x \approx 0.25\,\text{Å}^{-1}$ where L_x is the length of the box in the x direction. The power spectra of the surface charge densities are given as

$$S_{\mathrm{sol}}^{(\mathrm{s})}(q,\omega) = \frac{1}{\mathcal{A}} \int_{-\infty}^{+\infty} \mathrm{d}t \, \langle \tilde{n}_{\mathrm{sol}}^{(\mathrm{s})}(q,0)\, \tilde{n}_{\mathrm{sol}}^{(\mathrm{s})}(-q,t) \rangle \, e^{i\omega t}, \tag{S17}$$

and

$$S_{\mathrm{wat}}^{(\mathrm{s})}(q,\omega) = \frac{1}{\mathcal{A}} \int_{-\infty}^{+\infty} \mathrm{d}t \, \langle \tilde{n}_{\mathrm{wat}}^{(\mathrm{s})}(q,0)\, \tilde{n}_{\mathrm{wat}}^{(\mathrm{s})}(-q,t) \rangle \, e^{i\omega t}. \tag{S18}$$

Through the fluctuation-dissipation theorem, we can obtain the imaginary part of the surface response function through:

$$\mathrm{Im}\, g_{\mathrm{sol}}(q,\omega) = \frac{2\pi}{q} \frac{\omega}{2k_{\mathrm{B}}T} S_{\mathrm{sol}}^{(\mathrm{s})}(q,\omega), \tag{S19}$$

and

$$\mathrm{Im}\, g_{\mathrm{wat}}(q,\omega) = \frac{2\pi}{q} \frac{\omega}{2k_{\mathrm{B}}T} S_{\mathrm{wat}}^{(\mathrm{s})}(q,\omega). \tag{S20}$$

To ensure the spectrum is independent of noise, a Savitzky–Golay filter[25] was applied. The resulting spectra without further fitting are presented in the main article.

S2.3. Surface charge density autocorrelation function

To characterize relaxation of the solid and the liquid charge densities, we computed their respective normalized autocorrelation functions, defined as:

$$C_{\mathrm{sol}}^{(\mathrm{s})}(\tau;q) = \frac{\langle \tilde{n}_{\mathrm{sol}}^{(\mathrm{s})}(q,0)\, \tilde{n}_{\mathrm{sol}}^{(\mathrm{s})}(-q,\tau) \rangle}{\langle |\tilde{n}_{\mathrm{sol}}^{(\mathrm{s})}(q)|^2 \rangle}, \tag{S21}$$

and

$$C_{\mathrm{wat}}^{(\mathrm{s})}(\tau;q) = \frac{\langle \tilde{n}_{\mathrm{wat}}^{(\mathrm{s})}(q,0)\, \tilde{n}_{\mathrm{wat}}^{(\mathrm{s})}(-q,\tau) \rangle}{\langle |\tilde{n}_{\mathrm{wat}}^{(\mathrm{s})}(q)|^2 \rangle}. \tag{S22}$$

Again, focusing on the long-wavelength limit, we show the results for $C_{\mathrm{sol}}^{(\mathrm{s})}(\tau;q_0)$ and $C_{\mathrm{wat}}^{(\mathrm{s})}(\tau;q_0)$ in the main article.

S3. SENSITIVITY OF THE FRICTION COEFFICIENT

To assess the robustness of our results to the choice of simulation settings, here we present an extensive set of tests on the sensitivity of the friction coefficients computed to certain aspects of our simulations. In these tests, we show the results for two representative cases: $m_{\mathrm{D}} = 1$ amu for the weak-coupling regime and $m_{\mathrm{D}} = 5000$ amu for the strong-coupling regime.

S3.1. Convergence of the Green–Kubo friction coefficient

As seen from Fig. S2, the force autocorrelation $\langle \mathcal{F}(0)\mathcal{F}(\tau)\rangle$ shows oscillations due to charge density fluctuations in the solid at short timescales before decaying to zero at longer timescales. We can characterize two particular timescales: (i) the time at which the first minimum is reached, $\tau_{\mathrm{D}} \propto \omega_{\mathrm{D}}$, due to motion of the Drude oscillators and (ii) the force decorrelation time, $\tau_{\mathrm{F}} \propto \lambda$, as defined by Eq. S12. These are marked for the weak-coupling case in the inset of Fig. S2(a). In $\lambda_{\mathrm{GK}}(\tau)$, these timescales manifest in a peak at τ_{D} and a plateau after τ_{F}. In the weak-coupling regime where the Drude mass is low, there is a separation of timescales as $\tau_{\mathrm{D}} \ll \tau_{\mathrm{F}}$. A decrease in the solid charge density frequency in this regime only increases τ_{D} but not τ_{F}. The peak at τ_{D} is a local maximum, increasing in height as Drude mass increases, and a plateau is observed at times intermediate between τ_{D} and τ_{F}, unchanged in height. This is consistent with the converged friction coefficient remaining at $\lambda \approx 1.9 \times 10^4 \, \mathrm{N\,s\,m^{-3}}$. In the strong-coupling regime where the solid frequency is slow, τ_{D} is now comparable to τ_{F}. A decrease in the solid charge density frequency in this regime increases both τ_{D} and τ_{F}. As τ_{F} governs the value of λ_{GK} at long times, the converged friction coefficient now increases with decreasing charge density frequency. In order to get a consistent value for the friction coefficient, it is important to extract λ from $\lambda_{\mathrm{GK}}(\tau)$ at $\tau > \tau_{\mathrm{F}}$. Therefore, taking the maximum of $\lambda_{\mathrm{GK}}(\tau)$ as in some studies[23,26,27] is not appropriate, as also shown previously by Oga *et al.*[24]
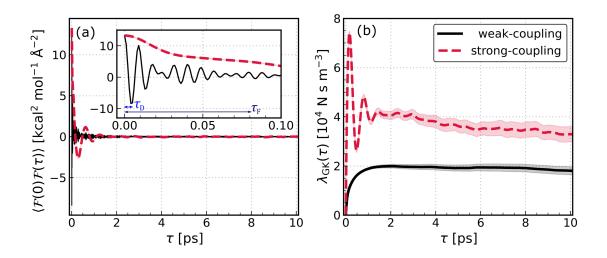

Figure S2. **Convergence of the Green–Kubo friction coefficient** (a) The force autocorrelation function of two representative cases in the weak-coupling and strong-coupling regimes. The inset shows clearer the oscillations due to the Drude dynamics. The memory time τ_{D} and the decay time τ_{F} are marked for the weak-coupling case. (b) The convergence of λ_{GK} where statistical errors (shaded area) are obtained from block-averaging.

For simulations with the largest Drude mass $m_{\mathrm{D}} = 10^7$ amu, we observe a plateau in $\lambda_{\mathrm{GK}}(\tau)$ from $\tau \gtrsim 5$ ps. Therefore, we give the converged friction coefficient in all cases to be the average of values of $\lambda_{\mathrm{GK}}(\tau)$ evaluated at correlation time between $5 < \tau/\mathrm{ps} < 10$.

S3.2. System size

To make sure the employed system size is sufficient to obtained converged values, we checked if our results remain consistent at larger system sizes. In Fig. S3, the friction coefficient for two representative Drude masses are shown for systems with different lateral areas in the (x, y) plane. The additional simulations were carried out on an interface with approximately the same liquid film thickness $\approx 37\,\text{Å}$. The friction coefficients computed from these simulations are almost identical to those presented in the main article.
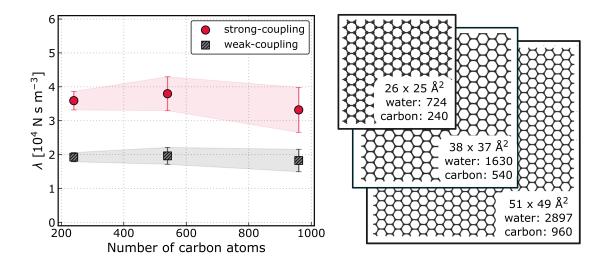

Figure S3. **Sensitivity of friction coefficient to system size.** Statistical errors are obtained from block-averaging. The three system sizes tested are illustrated on the right panel where only the solid sheets are shown. The corresponding total area for the sheet and the number of water molecules and carbon atoms are given for each system

S3.3. Simulation time

Analogous to checking the impact of system size, we checked the convergence of the friction coefficient with the simulation time length, as presented in Fig. S4. For all cases, the friction coefficient is found to change relatively little with increasing simulation time. While statistical errors are larger for shorter simulations, simulation times as short as 1 ns is enough to converge friction to within 10%. Therefore, the employed simulation time of 10 ns is sufficient for a converged friction coefficient.
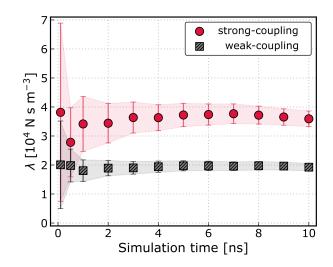
Figure S4. **Sensitivity of friction coefficient to simulation time.** λ changes relatively little with increasing simulation time. Statistical errors are obtained from block-averaging.

S3.4. Time-step

We test the sensitivity of the friction coefficients in both the weak-coupling and strong-coupling regimes with the time-step used in simulations and see that the results agree well for time-step of $0.1, 0.2, 0.5$ and $1\,\mathrm{fs}$, as shown in Fig. S5(a). However, when dealing with small Drude masses, problems with energy drifts often arise due to the inherently high frequency of the individual Drude oscillators.[1] We therefore also check that the time-step of $1\,\mathrm{fs}$ employed gives acceptable value of λ for Drude masses of $0.4 \leq m_\mathrm{D}/\mathrm{amu} \leq 5$ in our simulations, as shown in Fig. S5(b). Here, all these simulations belong to the weak-coupling regimes.
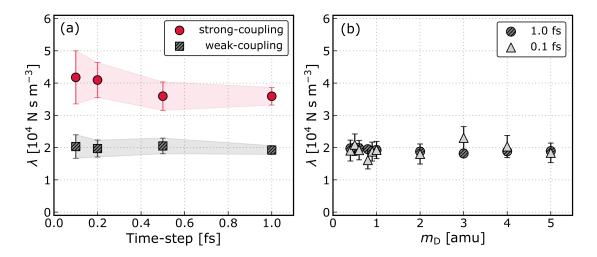

Figure S5. **Sensitivity of friction coefficient to time-step.** (a) Dependence of the computed λ on the time-step used in simulations. (b) Comparison of λ for simulations with $m_\mathrm{D} \lesssim 5\,\mathrm{amu}$ using a time-step of 0.1 and $1\,\mathrm{fs}$. Statistical errors are obtained from block-averaging.

Further analysis by extracting the static component, quantified by $\langle \mathcal{F}^2 \rangle$, and the dynamical component, quantified by τ_F, of the friction is shown in Fig. S6. This reveals that although λ converge for $m_\mathrm{D} \lesssim 2\,\mathrm{amu}$ for a time-step of $1\,\mathrm{fs}$, $\langle \mathcal{F}^2 \rangle$ and τ_F diverge for these small masses. Therefore, in the main article, $\langle \mathcal{F}^2 \rangle$ and τ_F for $m_\mathrm{D} \lesssim 2\,\mathrm{amu}$ cases are computed from simulations using a time-step of $0.1\,\mathrm{fs}$.
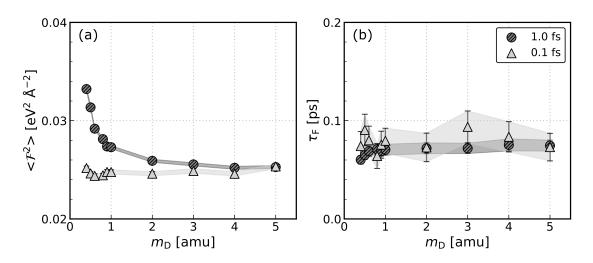
Figure S6. **Sensitivity of the static and dynamical components of friction to time-step.** Variation of (a) the mean squared force $\langle \mathcal{F}^2 \rangle$ and (b) the force decorrelation time τ_{F} for simulations with Drude masses $0.4 \leq m_{\mathrm{D}}/\mathrm{amu} \leq 5$ using a time-step of 0.1 and $1\,\mathrm{fs}$.

S3.5. Thermostats

Ordinarily, in simulations of polarizable systems using the classical Drude oscillator model, the temperature of the Drude particles is often kept low[1,3,28] to minimize energy exchange between the nuclear and Drude motion. In this work, we found numerical instabilities in simulations with low T_{sol} for $m_{\mathrm{D}} \gtrsim 10\,\mathrm{amu}$. Therefore, for all results presented in this work, we used two separate thermostats to keep the temperatures of the water, T_{wat}, and the Drude particles, T_{sol}, both at $300\,\mathrm{K}$. We carried out simulations with $m_{\mathrm{D}} = 1\,\mathrm{amu}$ (the weak-coupling regime) using different values for $T_{\mathrm{sol}} = 10, 100$ and $300\,\mathrm{K}$. As shown in Fig. S7, while the force autocorrelation function shows oscillations of greater magnitude at higher T_{sol}, its integral and therefore the friction coefficient is not significantly affected.
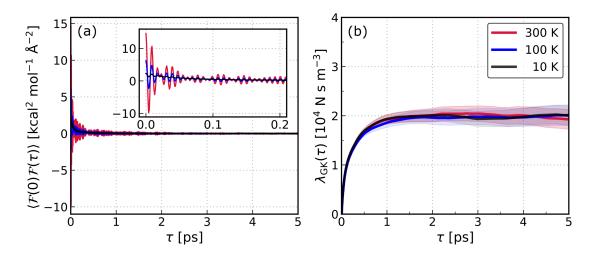

Figure S7. **Senstivity of friction coefficient to the temperature of the Drude particles.** (a) The force autocorrelation function for simulations with $m_{\mathrm{D}} = 1\,\mathrm{amu}$ where the Drude particles are kept at $T_{\mathrm{sol}} = 10, 100, 300\,\mathrm{K}$. The inset shows clearer the oscillations at short times. (b) The convergence of λ_{GK} for the three cases where statistical errors (shaded area) are obtained from block-averaging.

We also test the sensitivity of the friction coefficient to the thermostat settings used to maintain the temperature of the Drude particles. In Fig. S8, we show that the friction coefficients agree well for

different damping times of the Nosé–Hoover thermostat for the Drude particles $\tau_{\mathrm{NH}} = 1, 10, 100, 1000$ fs in both the weak-coupling and strong-coupling regimes. Equivalent results were also obtained with the canonical sampling through velocity rescaling (CSVR) thermostat.[29]
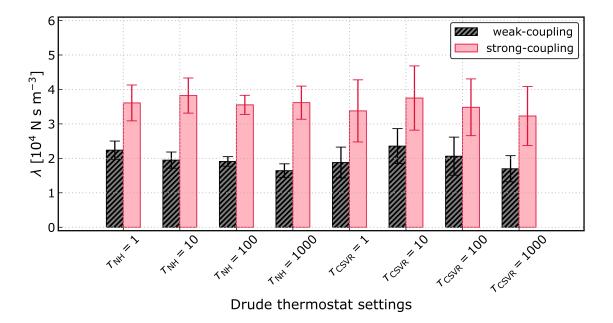

Figure S8. **Sensitivity of friction coefficient to thermostat settings for Drude particles.** The values of the damping time constant of the thermostat (τ_{NH} for the Nosé–Hoover thermostat and τ_{CSVR} for the CSVR thermostat) for the Drude particles are given in fs. Statistical errors are obtained from block-averaging.

S3.6. Liquid film thickness

Simulations for systems with varying thickness of the water film were performed to test the convergence of the friction coefficient. In Fig. S9(a), we show the planar average mass density profiles for the liquid–solid system with a water film of thickness $\approx 7, 17, 27, 37$ and 47 Å. The thickness is determined by the height from the positions of the carbon atoms in the sheet to where the water density at the liquid–vapour interface is equal to $0.5\,\mathrm{g\,cm^{-3}}$. In Fig. S9(b), we show how the extracted friction coefficient changes with the water film thickness. A water film with thickness $\gtrsim 17$ Å is required to have a region with bulk mass density and a converged friction coefficient. Therefore, employing a thickness of ≈ 37 Å for simulations of our main results is justified.
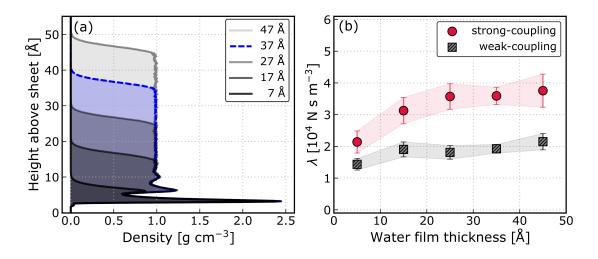
Figure S9. **Sensitivity of friction to simulation time to the liquid film thickness.** (a) The planar density profile of different film thicknesses above the flat solid sheet is shown for different water film thicknesses (indicated in the legend). In the main article, we use a thickness of ≈ 37 Å, as indicated by the dashed blue line. (b) The sensitivity of friction to the liquid thickness. Statistical errors are obtained from block-averaging.

S3.7. Electrostatic boundary conditions

For simulations presented in the main article, we treated electrostatics by applying the conventional three-dimensional Ewald summation (EW3D) technique.[30] This method is commonly employed in simulations of different interfacial systems.[23,31,32] To test the influence of this choice to the friction coefficient, we performed additional simulations with hybrid boundary conditions in which the Ewald summation is applied to the x and y directions while the electric displacement field in the z direction is set to zero ($D_z = 0$). This is done using the finite field approach[33–35] and such hybrid boundary conditions have been shown[33] to be formally equivalent to the Yeh–Berkowitz correction[36] that decouples the electrostatic interactions between a slab of material and its periodic images. We found good agreement for the friction coefficients of both the weak-coupling and strong-coupling regimes between the EW3D and the $D_z = 0$ methods, as shown in Fig. S10.
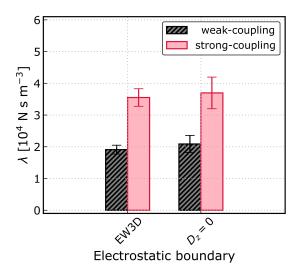

Figure S10. **Sensitivity of friction coefficient to electrostatic boundary conditions.** The friction coefficients in the weak-coupling and strong-coupling agree well for simulations employing the EW3D method and the $D_z = 0$ method. Statistical errors are obtained from block-averaging.

S4. SENSITIVITY OF THE DEPENDENCE OF FRICTION ON SOLID CHARGE DENSITY FREQUENCY

For the simulations presented in the main article, we fixed $Q_{\mathrm{D}} = 1.852\,e$ and $k_{\mathrm{D}} = 1000\,\mathrm{kcal\,mol^{-1}\mathring{A}^{-2}}$ for the Drude oscillators, which have been parameterized by Misra and Blanckstein to recover the polarizability tensor of a periodic graphene lattice.[14] In principle, Q_{D} and k_{D} both control the solid charge density and changing their values will affect the coupling between the solid and the liquid charge densities, and therefore the friction. Here we will present a check for the sensitivity of the dependence of friction on solid charge frequency upon changing to different values for each of these parameters.

S4.1. Varying the Drude charge

We performed two additional sets of simulations of the liquid–solid interface with $Q_{\mathrm{D}} = 0$ and $0.926\,e$ while keeping $k_{\mathrm{D}} = 1000\,\mathrm{kcal\,mol^{-1}\mathring{A}^{-2}}$ for Drude masses in the range $1 \lesssim m_{\mathrm{D}}/\mathrm{amu} \lesssim 10^{7}$ while other aspects of the simulations are kept the same. In the main article, we show the dependence of the friction on the frequency of the solid charge density by plotting λ against ω_0. Based on the discussion in Sec. S5, we can approximate the solid charge density as $\omega_0 \approx \omega_{\mathrm{D}}$ instead. Therefore, for convenience, in these additional analyses, λ is plotted against ω_{D} as shown in Fig. S11. The relationship mapped out for $Q_{\mathrm{D}} = 1.852\,e$ is essentially unchanged compared to the one presented in Fig. 2(a) in the main article.

For $Q_{\mathrm{D}} = 0$, there is no charge density in the solid, i.e $\tilde{n}_{\mathrm{sol}}(q, \omega) = 0$, so the only contribution to friction is from the surface roughness. Therefore the friction remains constant with ω_{D} at $\lambda \approx 1.7 \times 10^{4}\,\mathrm{N\,s\,m^{-3}}$ Increasing Q_{D} to 0.926 and $1.852\,e$ slightly increases the surface roughness contribution to friction, as seen from the flattening in the weak-coupling regime. Meanwhile, the contribution to friction from charge density coupling increases much more significantly in the strong-coupling regime for higher values of Q_{D}. This behavior supports the fact that the increase in friction at the low frequency end is indeed due to coupling of charge density between the solid and the liquid and larger charge density in the solid will couple more strongly with the liquid, resulting a larger increase in friction the strong-coupling regime.
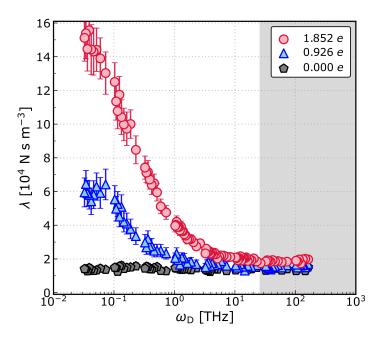

Figure S11. **Dependence of friction on solid charge density frequency for different Drude charges.** Values of Q_{D} are indicated in the legend and $k_{\mathrm{D}} = 1000\,\mathrm{kcal\,mol^{-1}\mathring{A}^{-2}}$ in all cases. The weak-coupling and strong-coupling regimes are shaded grey and not shaded, respectively. For simulations with $Q_{\mathrm{D}} = 0$, λ remains constant with ω_{D}. For simulations with $Q_{\mathrm{D}} = 0.926$ and $1.852\,e$, λ increases as ω_{D} is decreased in the strong-coupling regime.

S4.2. Varying the spring constant

Here, we performed two additional sets of simulations of the liquid–solid interface with $k_D = 600$ and $1000\,\mathrm{kcal\,mol^{-1}\mathring{A}^{-2}}$ while keeping $Q_D = 1.852\,e$, also for Drude masses in the range $1 \lesssim m_D/\mathrm{amu} \lesssim 10^7$, while other aspects of the simulations are kept the same.

Again, since the solid charge density is changed when k_D is varied, differences in the absolute values of λ are expected and indeed observed, as shown in Fig. S12. According to Eq. S6, a decrease in k_D means that the atom modeled by the Drude oscillator becomes less polarizable. Therefore, the friction contribution due to the surface roughness is higher for lower values of k_D but the differences in the λ in the weak-coupling regime are relatively small. The contribution to friction from charge density coupling is observed to be more strongly affected since λ increases much more sharply for lower k_D as ω_D is decreased in the strong-coupling regime. The important thing to stress is that this increase of λ due to charge density coupling in all cases occur once $\omega_D \lesssim \omega_{lib}$, supporting the separation into the weak-coupling and strong-coupling regimes in the main article.
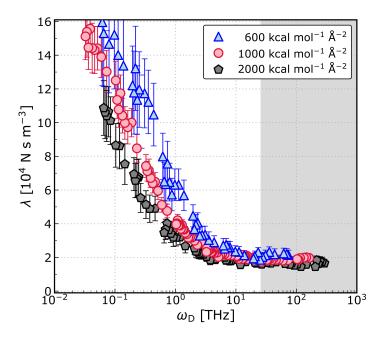

Figure S12. **Dependence of friction on solid charge density frequency for different harmonic force constant.** Values of k_D are indicated in the legend and $Q_D = 1.852\,e$ in all cases. The weak-coupling and strong-coupling regimes are shaded grey and not shaded, respectively. For all cases, λ increases once $\omega_D \lesssim \omega_{lib}$ in the strong-coupling regime.

S4.3. Flexible water model

To check the sensitivity of our results to the presence of intramolecular modes in water, we performed additional simulations with a flexible water model SPC/Fw.[37] In additional to the intermolecular librational and Debye modes, SPC/Fw also captures the OH stretching modes as a peak centered at $\approx 100\,\mathrm{THz}$ and in-plane bending modes as a peak centered at $\approx 50\,\mathrm{THz}$. The addition of these peaks in the water dielectric spectrum does not affect the conclusions drawn in the main article, as shown in Fig. S13.
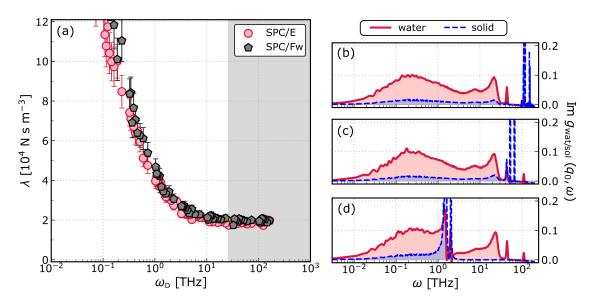
Figure S13. **Dependence of friction on solid charge density frequency for a flexible water model.** (a) The friction dependence on ω_{D} remains almost unchanged when simulations are performed with a rigid (SPC/E) or flexible (SPC/Fw) water model. When solid principal peaks coincide with (b) the OH stretching modes or (c) the in-plane stretching mode, there is no significant response in either the solid or the liquid. (d) The strong-coupling regime remains at frequencies lower than the librational peak.

S4.4. Phonon contribution

In this work, we do not consider the effect of phonons in the solid on the friction of the interface, which would in principle affect both the surface roughness contribution λ_{SR} and the contribution from the coupling of the dynamics of the solid and the liquid λ_{THz}. Here, we can simply investigate how a single phonon mode in the solid would change the friction. We do this by considering a simple model in which the solid is a set of independent harmonic oscillators whereby the carbon atoms are now attached to their lattice positions via a harmonic spring with force constant k_{ph}, and ascribed a mass m_{ph}. The carbon atoms still interact with the water through the same Lennard-Jones potential. By varying m_{ph} we can tune the phonon frequency $\omega_{\mathrm{ph}} = (k_{\mathrm{ph}}/m_{\mathrm{ph}})^{1/2}$ (with $k_{\mathrm{ph}} = 1000\,\mathrm{kcal\,mol^{-1}\,\mathring{A}^{-2}}$) in a similar fashion to how we tuned the solid's dielectric spectrum. In contrast to varying m_{D}, we see that friction is relatively insensitive to changes in m_{ph}, as seen in Fig. S14. This result is in line with the prediction of QF theory that, for water at carbon substrates, phonon contributions to quantum friction are relatively small.
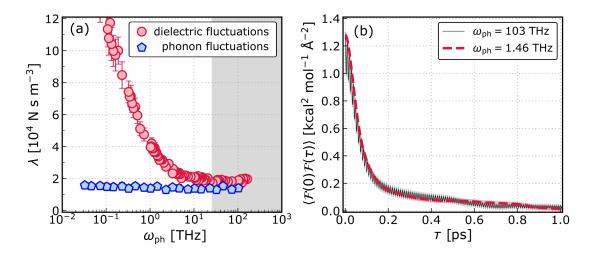
Figure S14. **Dependence of the friction on the phonon mode frequency.** (a) The friction is not strongly affected by phonon fluctuations compared to the effect seen for dielectric fluctuations in the the solid. (b) The force–force autocorrelation functions are shown for two different phonon frequencies as indicated in the legend. Unlike for dielectric modes, the phonon modes do not change the force decorrelation time significantly.

S5. COUPLING OF CHARGE DENSITIES

In this section, we present further analyses of the surface response functions of the solid and the liquid in support of the conclusions made on the separation into the weak-coupling and strong-coupling regimes in the main article.

S5.1. Solid surface response function in the absence of water

In the main article, we show that the surface response function of the solid $g_{sol}(q_0, \omega)$ is dominated by two peaks that are slightly blue-shifted from ω_D. Here we provide more details into the origin of each of these peaks, with the peak lower in frequency denoted as ω_0 and the peak higher in frequency denoted as ω_1.

In the absence of the Coulomb interaction, the Drude oscillators are simply a set of independent harmonic oscillators characterized by a single frequency ω_D. In the presence of the Coulomb interaction, the motion of the Drude oscillators is no longer isotropic, with motion perpendicular to the plane of the graphene sheets having a higher frequency (ω_1) than parallel motion (ω_0). To illustrate this point further, in Fig. S15(b), we show how $g_{sol}(q_0, \omega)$ changes as the force constants of the springs are changed to $(k_{xy}, k_z) = (4k_D, k_D)$ and $(k_{xy}, k_z) = (k_D, 4k_D)$, where $k_D = 1000 \, \text{kcal} \, \text{mol}^{-1} \, \text{Å}^{-2}$. (To be clear, in the main article, an isotropic spring constant k_D is used throughout.) When $(k_{xy}, k_z) = (4k_D, k_D)$, ω_0 shifts to higher frequency and ω_1 is unaffected. Conversely, when $(k_{xy}, k_z) = (k_D, 4k_D)$, ω_1 shifts to higher frequency and ω_0 position is unaffected.
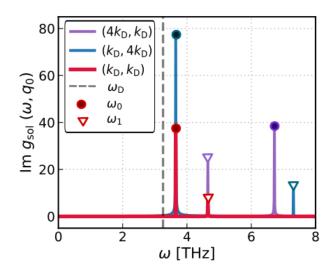

Figure S15. **Solid surface charge density in the absence of water.** The surface response function $g_{sol}(q_0, \omega)$ of a carbon sheet with Drude particles of mass $m_D = 10^3$ amu such that $\omega_D = (k_D/m_D)^{1/2} = 3.3 \, \text{THz}$ in the absence of water. The value of ω_D is marked with a dashed vertical line. When the spring is changed from having an isotropic force constant $(k_{xy}, k_z) = (k_D, k_D)$ to an anisotropic one, the modes in $g_{sol}(q_0, \omega)$ are shifted accordingly. When $(k_{xy}, k_z) = (4k_D, k_D)$, the parallel mode at ω_0 (denoted with a filled circle) is shifted. When $(k_{xy}, k_z) = (k_D, 4k_D)$, the perpendicular mode at ω_1 (denoted with an empty triangle) is shifted.

To access the dispersion relation of the solid modes in more detail, we perform simulations of the solid system with a supercell length of $153.36 \, \text{Å}$. In Fig. S16(a), we show $g_{sol}(q, \omega)$ in both q-space and ω-space. Both the solid modes show relatively flat dispersion, with very narrow widths in ω-space and spanning up to $q_{max} \approx 1.5 \text{Å}^{-1}$ in q-space. This flat dispersion of the solid modes is seen in simulations with different values of ω_D, as illustrated in Fig. S16(b).
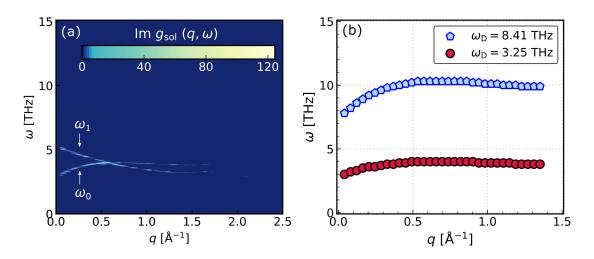
Figure S16. **Dispersion relation of the solid modes.** (a) The solid surface response $g_{sol}(q,\omega)$ of a carbon sheet with Drude particles of mass $m_D = 10^3$ amu in the absence of water. The tangential mode increases in frequency while the perpendicular mode decreases in frequency before flattening out up to $q_{max} \approx 1.5 \text{Å}^{-1}$. (b) The solid tangential mode shows relatively flat dispersion relation, as shown for two representative simulations with ω_D indicated in the legend.

S5.2. Solid surface response function in the presence of water

In the absence of water, there are two sources of dissipation in the solid as the Drude oscillators are coupled to a thermostat and also interact with each other by electrostatic interactions. Therefore, the principal modes in the solid have finite widths in the response function. However, since the Drude oscillators are only weakly-coupled, they remain underdamped and these widths remain very small. In the presence of water, when there is strong-coupling with the intermolecular modes of water, the Drude oscillators are more strongly damped, leading to the broadening of their widths.

Focusing on the case when $\omega_D = 3.26$ THz, we can quantify this broadening by fitting the surface response function $g_{sol}(q_0,\omega)$ obtained from simulations to a double-Lorentzian

$$\text{Im}\, g_{sol}(q_0,\omega) = \frac{a_0\eta_0^2}{(\omega-\omega_0)^2+\eta_0^2} + \frac{a_1\eta_1^2}{(\omega-\omega_1)^2+\eta_1^2}, \tag{S23}$$

where a_0 is the amplitude, ω_0 is the centered frequency, η_0 is the width of the tangential mode and a_1, ω_1, η_1 are similarly defined for the perpendicular mode. The results obtained for the fitting parameter are given in Table S3. We see that both of the principal modes experience a small redshift to lower frequency of ≈ 0.06 THz. More prominently, the amplitudes of both peaks are reduced and the widths are broadened in the presence of water.

	a_0	ω_0 [THz]	η_0 [THz]	a_1	ω_1 [THz]	η_1 [THz]
without water	17	4.65	0.0032	36	3.65	0.0020
with water	0.68	4.59	0.154	0.82	3.49	0.1742

Table S3. **Parameters for fitting the solid surface response to a double-Lorentzian as Eq. S23.**

In Figs. S17, we show the fitted $g_{sol}(q_0,\omega)$ profile for simulations of the solid with various values of m_D in the absence and in the presence of water. While the principal peaks remain at $\omega_0 \approx \omega_1 \approx \omega_D$ in all cases, they begin to broaden and decrease in height more significantly for cases in the strong-coupling regime.
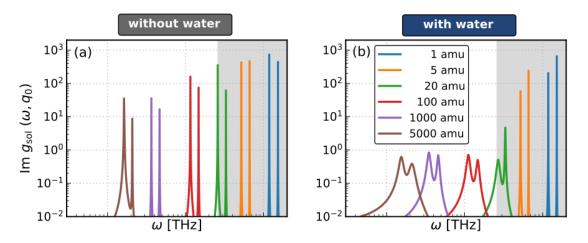
Figure S17. **Solid peaks broaden in the presence of water.** The solid surface response function fitted to a double-Lorentzian function for a range of different m_D (as indicated in the legend) in the (a) absence and (b) presence of water.

S5.3. Water surface response function

For the water surface response in the weak-coupling regime, we focus on $g_{wat}(q, \omega)$ obtained from simulations with $m_D = 1\,$u here as shown in Fig. S18(a). However, the result pertains to all simulations with $m_D \lesssim 20\,$u. At the long wavelength limit ($q \to 0$), we see that water shows a sharp peak at $\omega_{lib} \approx 20\,$THz coming from the librational modes and a broad feature spanning $10^{-2} - 10^{1}$ THz. The dielectric fluctuations due to intermolecular modes of water in this regime agree well with previous simulations with different interaction potentials.[38] As q is increased, we see a decrease in $g_{wat}(q, \omega)$. Most importantly, in the weak-coupling regime, the water response function appears unperturbed by the presence of the Drude particles at all wavevectors.

In the strong-coupling regime, we focus on $g_{wat}(q, \omega)$ obtained from simulations with $m_D = 5000\,$u. As shown in Fig. S18(b), at the long wavelength limit ($q \to 0$), we see that $g_{wat}(q, \omega)$ is strongly perturbed, indicating that the water and the Drude particles' motions are strongly coupled. As q increases above $q \approx 1.5\,\text{Å}^{-1}$, this coupling becomes less significant, which is consistent with $g_{sol}(q, \omega)$ decays for $q \gtrsim 1.5\,\text{Å}^{-1}$.
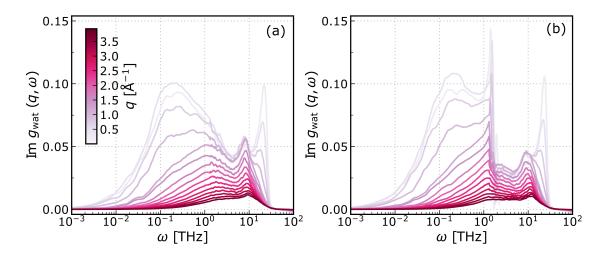

Figure S18. **Water surface response function.** $g_{wat}(q, \omega)$ obtained from simulations (a) in the weak-coupling regime appears unperturbed by the presence of the Drude oscillators. (b) In the strong-coupling regime, $g_{wat}(q, \omega)$ is strongly perturbed by the solid up to $q \approx 1.5\,\text{Å}^{-1}$.

S5.4. Force spectra

To further illustrate the change from the weak-coupling to the strong-coupling regime, we also computed the spectrum of the lateral force defined as

$$S_{\mathrm{F}}(\omega) = \int_{-\infty}^{+\infty} dt \, \langle \mathcal{F}(0)\mathcal{F}(t) \rangle \, e^{i\omega t}. \tag{S24}$$

We show $S_{\mathrm{F}}(\omega)$ for simulations with Drude masses used the previous subsection in conjunction with the Green–Kubo friction $\lambda_{\mathrm{GK}}(\tau)$ in Fig. S19. For cases belonging to the weak-coupling regime ($m_{\mathrm{D}}/\mathrm{amu} = 1, 2$, and 5), $S_{\mathrm{F}}(\omega)$ shows a peak due to the solid charge density at $\omega \approx \omega_0$ determined from $S_{\mathrm{sol}}(q_0, \omega)$, and a broad feature at low ω from the water charge density. As m_{D} is increased, the peak due to the solid starts to merge with the water broad feature and increase in intensity. This can be linked to the behavior of $\lambda_{\mathrm{GK}}(\tau)$ in the strong-coupling regime ($m_{\mathrm{D}}/\mathrm{amu} = 20, 50, 200, 1000$ and 5000): the increase in $S_{\mathrm{F}}(\omega = \omega_0)$ is responsible for stronger oscillations in $\lambda_{\mathrm{GK}}(\tau)$ at shorter times ($\tau < \tau_{\mathrm{F}}$) while the increase in $S_{\mathrm{F}}(\omega \lesssim \omega_0)$ is responsible for a higher plateau value at longer times ($\tau \geq \tau_{\mathrm{F}}$).
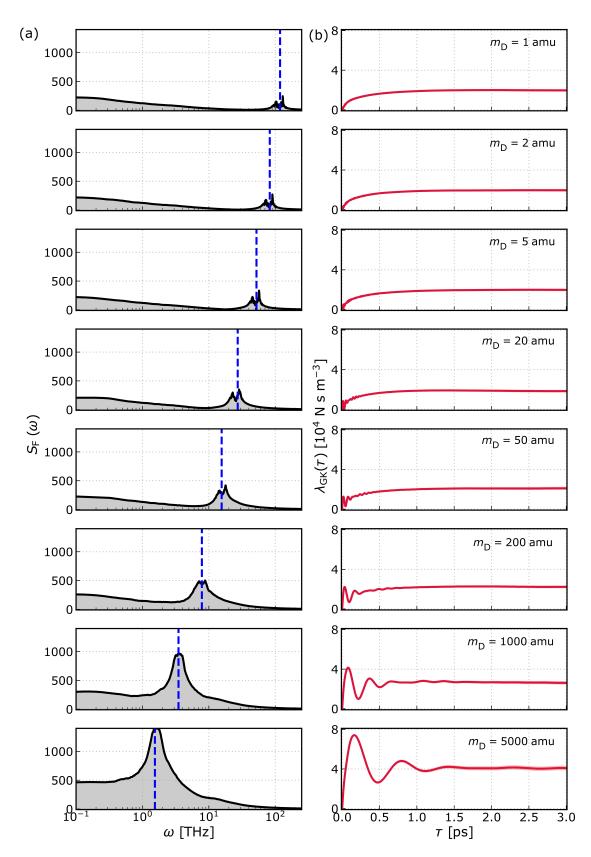
Figure S19. **Lateral force spectra.** (a) $S_F(\omega)$ for simulations with different m_D. The value of ω_0 extracted from $S_{sol}(q_0, \omega)$, marked as a dashed blue line, match with the frequency of the peak in $S_F(\omega)$ due to solid charge density contribution. This peak shows higher intensity as we move from the weak-coupling regime ($m_D < 20$ amu) to the strong-coupling regime ($m_D \geq 20$ amu). (b) This change manifests in $\lambda_{GK}(\tau)$ as the appearance of small oscillations at short τ and the increase in the plateau value at longer τ.

S6. COMPARISON TO QUANTUM FRICTION THEORY

S6.1. Quantum friction formula

In quantum friction theory,[38] Kavokine *et al.* derived an expression for the QF coefficient given as

$$\lambda_Q = \frac{\hbar^2}{8\pi^2 k_B T} \int_0^\infty dq\, q^3 \int_0^\infty d\omega\, \frac{1}{\sinh^2(\hbar\omega/2k_B T)} \frac{\operatorname{Im} g_{sol}(q,\omega) \operatorname{Im} g_{wat}(q,\omega)}{|1 - g_{sol}(q,\omega)\, g_{wat}(q,\omega)|^2}, \tag{S25}$$

where $g_{sol}(q,\omega)$ and $g_{wat}(q,\omega)$ are the surface response functions for the solid and water in the absence of any coupling respectively.

S6.2. Water surface response

To evaluate λ_Q quantitatively, one needs to obtain $g_{sol}(q,\omega)$ and $g_{wat}(q,\omega)$. As in Ref. 38, the water dielectric function is represented by a sum of two Debye peaks at $\omega_{Db,1}$ and $\omega_{Db,2}$, each with an exponentially decaying q dependence

$$g_{wat}(q,\omega) = \frac{g_{wat}(q,0)}{2} \left(\frac{e^{-q/q_0}}{1 - i\omega/\omega_{Db,1}} + \frac{2 - e^{-q/q_0}}{1 - i\omega/\omega_{Db,2}} \right), \tag{S26}$$

where $g_{wat}(q,\omega)$ is given as

$$g_{wat}(q,0) = e^{a+b[1+(q/c)^d]^{1/d}}. \tag{S27}$$

We have used the same parameters as Ref. 38, which for completeness, are reproduced in Table S4.

$g_{wat}(q,\omega)$	Werder $g_{wat}(q,0)$	Aluru $g_{wat}(q,0)$
$q_0 = 3.12\,\text{Å}^{-1}$	$a = 5.16$	$a = 3.38$
$\omega_{Db,1} = 0.36\,\text{THz}$	$b = -5.19$	$b = -3.41$
$\omega_{Db,2} = 4.84\,\text{THz}$	$c = 1.95\,\text{Å}^{-1}$	$c = 1.79\,\text{Å}^{-1}$
	$d = 2$	$d = 2.4$

Table S4. **Parameters for the analytical expression for the water surface response function in the absence of charge density coupling from the solid.**

For the solid dielectric fluctuations, two different models were used to represent the graphite's dispersionless surface plasmon. Numerical evaluation in Ref. 38 of the QF coefficient using the Aluru $g_{wat}(q,\omega)$ gave a contribution of $\lambda_Q \approx 0.5 \times 10^4\,\text{N\,s\,m}^{-3}$ with a "Drude" model for the surface plasmon, which is comparable to λ_{THz} obtained from our simulations.

S6.3. Solid surface response with reparameterized Drude model

Encouraged by the agreement between λ_{THz} obtained from simulations and λ_Q predicted from QF theory, we can further assess how well our simulations are capturing QF by reparameterizing the Drude model to approximately represent the surface response function of our simple model. In the Drude model for a surface plasmon, which is based on the semi-classical treatment of free electron dynamics,[39] the solid surface response function is of the form

$$g_{sol}(q,\omega) = \frac{\omega_p^2}{\omega_p^2 - \omega^2 - 2i\eta\,\omega}\Theta(q_{max} - q), \tag{S28}$$

where ω_p is the principal peak due to the plasmon, η is the surface plasmon width, Θ is the Heaviside step function and q_{max} is the cut-off wavevector.

Drawing a parallel mapping to the surface response function obtained in our simulations, we can parameterize the Drude model to represent a surface plasmon with frequency $\omega_{\mathrm{p}} = \omega_0$ corresponding to the principal tangential mode in simulations. We choose $\eta = \omega_0/100$ and $q_{\max} = 1.5\,\text{Å}^{-1}$, giving $\mathrm{Im}\,g_{\mathrm{sol}}(q < 1.5\,\text{Å}^{-1}, \omega = \omega_{\mathrm{p}}) = 50$, such that the plasmon has a small width and long flat dispersion, and its surface response function matches reasonably well with that obtained in simulations (Fig. S16).

S6.4. Comparison of the quantum friction coefficient

Using the reparameterized Drude model for the solid surface response function and the Werder water surface response function, we evaluated the QF coefficient λ_{Q} from Eq. S25. For a plasmon mode with $\omega_{\mathrm{p}} = 10\,\text{THz}$, the reparameterized Drude model gives $\lambda_{\mathrm{Q}} \approx 0.2 \times 10^4\,\text{N s m}^{-3}$. This is close to the value obtained with the Drude model in Ref. 38 and the quantitative difference can be explained by comparing the contribution of the integrand of Eq. S25, $\tilde{\lambda}_{\mathrm{Q}}$, in (q, ω) space, as shown in Fig. S20.
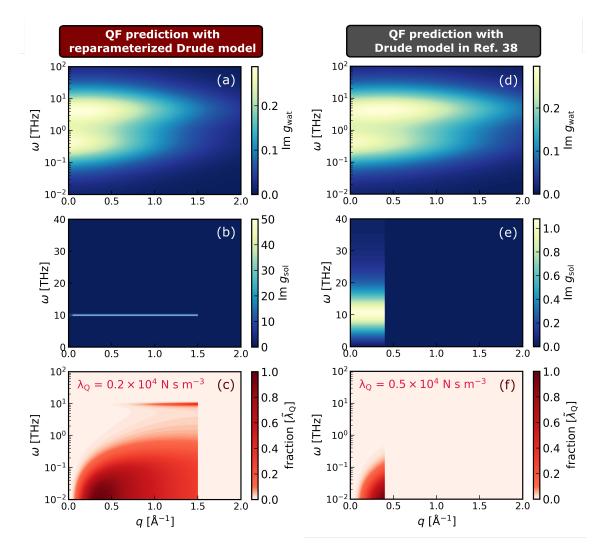

Figure S20. **Comparison of the quantum friction coefficient with parameters from simulations (a-c) and from Ref. 38 (d-f).** (a) The water Werder surface response function. (b) The solid surface response function from the reparameterized Drude model. (c) The QF integrand contributes mainly at $(\omega \lesssim 1\,\text{THz}, q < 1.5\,\text{Å}^{-1})$ and at $(\omega \approx \omega_{\mathrm{p}} = 10\,\text{THz}, 1 < q/\text{Å}^{-1} < 1.5)$. (d) The water Aluru surface response function. (e) The solid surface response function from the Drude model with parameters from Ref. 38. (f) The QF integrand contributes mainly at $(\omega \lesssim 0.1\,\text{THz}, q < 0.5\,\text{Å}^{-1})$.

Since there is little difference between the water surface response functions $g_{\mathrm{wat}}(q, \omega)$ in the two cases, the difference comes down to the solid surface response $g_{\mathrm{sol}}(q, \omega)$ or ultimately the plasmon dispersion. Since the plasmon in the reparameterized Drude model spans to a higher wavevector compared to the Drude model in Ref. 38, $\tilde{\lambda}_{\mathrm{Q}}$ contributes significantly to the final integral not only at ($\omega \lesssim 1\,\mathrm{THz}$, $q < 1.5\,\text{\AA}^{-1}$) but also at ($\omega \approx \omega_{\mathrm{p}} = 10\,\mathrm{THz}$, $1 < q/\text{\AA}^{-1} < 1.5$). However, since the width of the plasmon in the reparameterized Drude model is much smaller, the final integral value for λ_{Q} is still smaller.

S6.5. Sensitivity of the dependence of quantum friction on the solid frequency

From QF theory, we can also map out the dependence of the QF friction coefficient as a function of frequency of the solid mode. Using the reparameterized Drude model, as presented in the main article, we see a very good agreement between λ_{Q} calculated from theory and λ_{THz} obtained from simulations in the frequency range where graphite surface plasmons are experimentally observed.

In the Drude model, both the width η and the wavevector cut-off q_{max} control the plasmon dispersion and changing their values will affect the solid surface response function $g_{\mathrm{sol}}(q, \omega)$ and therefore the friction. We can also check the sensitivity of the dependence of the QF coefficient on the plasmon frequency upon changing to different values for each of these parameters. In simulations with the solid modes' frequencies in the range $2 - 20\,\mathrm{THz}$ where graphite's surface plasmons are experimentally observed, the solid modes' wavevector cut-offs can sensibly range between $q_{\mathrm{max}} \approx 1.4 - 2.0\,\text{\AA}^{-1}$ and their amplitudes can sensibly range between $\mathrm{Im}\, g_{\mathrm{sol}}(q < q_{\mathrm{max}}, \omega = \omega_{\mathrm{p}}) \approx 30 - 100$. This corresponds to $\eta/\omega_0 \approx 1/60 - 1/200$ in the Drude model. In Fig. S21(a), we show the dependence of QF on ω_0 using the Drude model for different values of q_{max} while keeping the width at $\eta = \omega_0/100$. As q_{max} increases, there is a higher contribution to the QF integral at higher q, leading to a higher λ_{Q}. In Fig. S21(b), we show again this dependence for different values of the width η/ω_0 while while keeping the wavevector cut-off at $q_{\mathrm{max}} = 1.5\,\text{\AA}^{-1}$. As η/ω_0 increases, the width of the plasmon decreases, leading to lower values of λ_{Q}. In all cases, however, there is only a significant contribution to QF when $\omega_0 \lesssim 20\,\mathrm{THz}$, which agrees with the results in the strong-coupling regime from simulations.
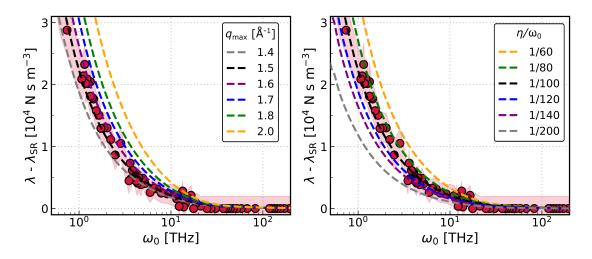

Figure S21. **Dependence of the quantum friction coefficient on the solid charge density frequency from the Drude model** (a) for different values of q_{max} (indicated in the legend) while keeping $\eta = \omega_0/100$ and (b) for different values of η/ω keeping $q_{\mathrm{max}} = 1.5\,\text{\AA}^{-1}$. The calculated λ_{Q} from theory is shown with dashed lines while λ_{THz} extracted from simulations are shown as red points with the shaded red region as the error from block-averaging.

S7. ADDITIONAL PROPERTIES OF THE INTERFACE

S7.1. Static properties

For static properties in the liquid, we analyse the density profiles of the water along the surface normal. These are identical for the weak-coupling and the strong-coupling cases, as shown in Fig. S22(a). In the solid, the magnitude of the dipole moment of a Drude oscillator can be obtained from $\mu_D = Q_D d$ where d is the distance of the Drude particle from the core atom. We look at its probability distribution $p(\mu_D)$ for both cases, as shown in Fig. S22(b). In both cases, $p(\mu_D)$ is identical, reinforcing that the interatomic potential, and therefore all static equilibrium properties of the interface are not affected when m_D is varied.
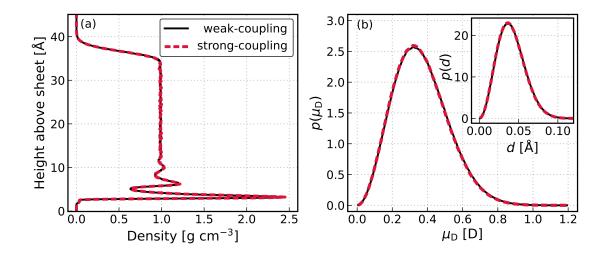

Figure S22. **Static equilibrium properties.** (a) The planar mass density profiles of the water are identical for the weak-coupling and the strong-coupling cases, showing a maximum density of $\approx 2.5\,\mathrm{g\,cm^{-3}}$ and is at a height $\approx 3.2\,\text{Å}$ for the contact layer of water. (b) The probability distributions of the dipole moment magnitude of a Drude oscillator $p(\mu_D)$ in the solid are also identical for both cases, with the average of the distribution at $\langle \mu_D \rangle \approx 0.36\,\mathrm{D}$. The inset shows the distribution of the distance between the Drude particles and their cores $p(d)$.

To link these observations to the unchanged static component of the friction coefficient described in the main article, we also look at the corrugation of the free energy surface (FES) experienced by the water molecules. Following previous work,[22,40,41] the two-dimensional FES of species i is given by

$$\Delta G_i(x,y) = -k_B T \ln[p_i(x,y)], \tag{S29}$$

where $p_i(x,y)$ is the normalized two-dimensional probability of finding species i in the contact layer at point (x,y). For every saved configuration, we define the contact layer as consist of water molecules with height above the sheet $\leq 5\,\text{Å}$, where the first minimum in the density profile is. After computing both $p_O(x,y)$ and $p_H(x,y)$ and averaging onto a unit cell in the solid, we obtained the oxygen-based and hydrogen-based FESs. To ensure each surface is independent of noise, a Savitzky–Golay filter[25] was applied. The corrugation of each FES, ΔG_O and ΔG_H, can be quantified by taking the highest free energy present in the FES. As shown in Fig. S23, the water molecules experience the same oxygen-based and hydrogen-based FES at the liquid–solid interface in the weak-coupling and the strong-coupling regimes. Since corrugation is much more pronounced in the oxygen-based FES, we show ΔG_O as an approximation of the total corrugation in the main article.
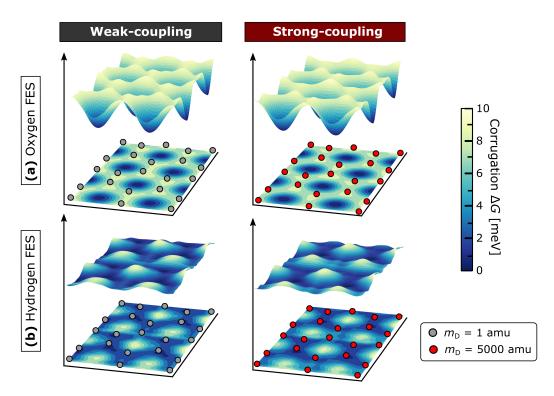
Figure S23. **Free energy surface corrugation** (a) The oxygen-based FES shows that oxygen atoms preferentially sit on hollow sites in the middle of the hexagon rings in graphene. (b) The hydrogen-based FES, which is less corrugated than the oxygen-based FES, shows that hydrogen atoms preferentially sit on carbon sites. The solid atoms are represented by the markers in the projection where the core atom in the Drude oscillator with $m_D = 1$ amu is in grey and $m_D = 5000$ amu in red. Both FESs show identical level of corrugation in the weak-coupling and strong-coupling cases.

S7.2. Charge density relaxation in the water film

Instead of looking at the charge density relaxation at just the surface, we can also characterize the relaxation of the whole water film. We can define the Fourier components of the charge densities for the solid and the liquid as

$$\tilde{n}_{\text{sol}}(q,t) = \sum_{\alpha \in \text{sol}} Q_\alpha e^{i\boldsymbol{q}\cdot\boldsymbol{x}_\alpha(t)}, \tag{S30}$$

$$\tilde{n}_{\text{wat}}(q,t) = \sum_{\alpha \in \text{wat}} Q_\alpha e^{i\boldsymbol{q}\cdot\boldsymbol{x}_\alpha(t)}, \tag{S31}$$

where we have implicitly only considered the zero wavevector in the direction normal to the graphene sheet. We can again characterize the relaxation of these charge densities with the following autocorrelation functions

$$C_{\text{sol}}(\tau;q) = \frac{\langle \tilde{n}_{\text{sol}}(q,0)\,\tilde{n}_{\text{sol}}(-q,\tau)\rangle}{\langle |\tilde{n}_{\text{sol}}(q)|^2\rangle}, \tag{S32}$$

$$C_{\text{wat}}(\tau;q) = \frac{\langle \tilde{n}_{\text{wat}}(q,0)\,\tilde{n}_{\text{wat}}(-q,\tau)\rangle}{\langle |\tilde{n}_{\text{wat}}(q)|^2\rangle}. \tag{S33}$$

Focusing on the long-wavelength limit, we show the results for $C_{\text{sol}}(\tau;q_0)$ and $C_{\text{wat}}(\tau;q_0)$ in Fig. S24. Again, the solid modes relax on a much faster timescale in the strong- than in the weak-coupling regime.

The water relaxation, however, barely differs between the two regimes, meaning any response in the liquid due to coupling with the Drude motions is localized the surface and does not affect the response of the whole film of water significantly as a whole.
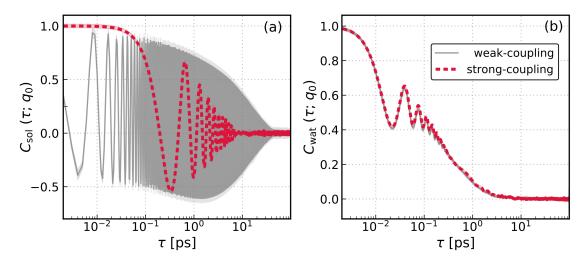

Figure S24. **Charge density correlation: asymmetry in response between the liquid and the solid.** (a) The relaxation of the solid charge density is much faster in the strong-coupling than the weak-coupling regime while (b) relaxation of the charge density of the whole water film barely differs between the two regimes.

S7.3. Other dynamical properties

In addition to the charge density relaxation, we also explored other dynamical properties of water including its orientational relaxation and hydrogen-bonding relaxation. The orientational dynamics of water molecules in the liquid is examined, following Yeh and Mou,[42] via the second-order rotational autocorrelation function, defined as

$$C_{\rm rot}(\tau) = \langle P_2[\boldsymbol{u}(0) \cdot \boldsymbol{u}(\tau)]\rangle, \tag{S34}$$

where $\boldsymbol{u}(\tau)$ is the unit vector along the water molecular dipole at time τ and $P_2(x)$ denotes the second Legendre Polynomial. The hydrogen-bond relaxation is examined via the autocorrelation function of the presence of a hydrogen bond, defined as

$$C_{\rm hb}(\tau) = \frac{\langle h(0) \cdot h(\tau)\rangle}{\langle h^2\rangle}, \tag{S35}$$

where $h(\tau) = 1$ if there is a hydrogen bond between a pair of water molecules at time τ and $h(\tau) = 0$ otherwise. Two water molecules are considered to be hydrogen-bonded according to geometric criteria from Luzar and Chandler.[43]
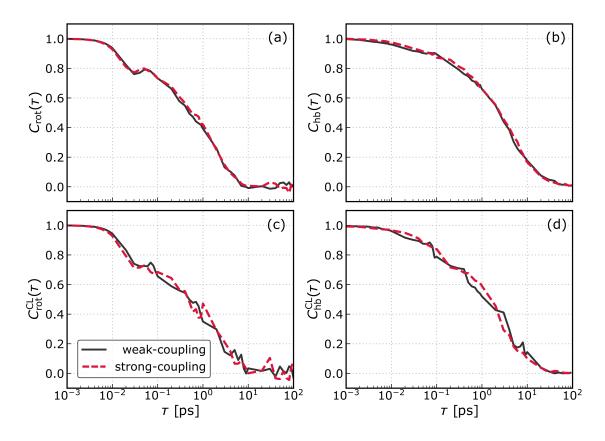
Figure S25. **Dynamical properties of water.** The rotational autocorrelation (a and c) and the hydrogen-bonding autocorrelation (b and d) are both barely affected between the weak-coupling and the strong-coupling regimes. The functions are computed for the whole water film (a and b) and just the contact layer (c and d).

From Figs. S25(a) and (b), we see little differences between the weak-coupling and strong-coupling cases for both $C_{\mathrm{rot}}(\tau)$ and $C_{\mathrm{hb}}(\tau)$ computed for the whole water film. These observations still hold when we look at $C_{\mathrm{rot}}^{\mathrm{CL}}(\tau)$ and $C_{\mathrm{hb}}^{\mathrm{CL}}(\tau)$, in Figs. S25(c) and (d), where superscript CL denotes that the autocorrelation functions are defined for just the contact layer (defined as the layer from the carbon sheet up to the first minimum of the water density profile). This supports our conclusion that the increase in friction due to charge density coupling has little impact on local dynamical properties of the liquid.

REFERENCES

[1] G. Lamoureux and B. Roux, "Modeling induced polarization with classical Drude oscillators: Theory and molecular dynamics simulation algorithm," The Journal of Chemical Physics **119**, 3025–3039 (2003).

[2] B. T. Thole, "Molecular polarizabilities calculated with a modified dipole interaction," Chemical Physics **59**, 341–350 (1981).

[3] C. Schröder and O. Steinhauser, "Simulating polarizable molecular ionic liquids with Drude oscillators," The Journal of Chemical Physics **133**, 154511 (2010).

[4] S. Y. Noskov, G. Lamoureux, and B. Roux, "Molecular dynamics study of hydration in ethanolwater mixtures using a polarizable force field," The Journal of Physical Chemistry B **109**, 6705–6713 (2005).

[5] G. Lamoureux, E. Harder, I. V. Vorobyov, B. Roux, and A. D. MacKerell, "A polarizable model of water for molecular dynamics simulations of biomolecules," Chemical Physics Letters **418**, 245–249 (2006).

[6] J.-L. Barrat and L. Bocquet, "Influence of wetting properties on hydrodynamic boundary conditions at a fluid/solid interface," Faraday Discuss. **112**, 119–128 (1999).

[7] K. Falk, F. Sedlmeier, L. Joly, R. R. Netz, and L. Bocquet, "Ultralow liquid/solid friction in carbon nanotubes: Comprehensive theory for alcohols, alkanes, OMCTS, and water," Langmuir **28**, 14261–14272 (2012).

[8] S. Plimpton, "Fast parallel algorithms for short-range molecular dynamics," Journal of Computational Physics **117**, 1–19 (1995).

[9] A. P. Thompson, H. M. Aktulga, R. Berger, D. S. Bolintineanu, W. M. Brown, P. S. Crozier, P. J. in 't Veld, A. Kohlmeyer, S. G. Moore, T. D. Nguyen, R. Shan, M. J. Stevens, J. Tranchida, C. Trott, and S. J. Plimpton, "LAMMPS - a flexible simulation tool for particle-based materials modeling at the atomic, meso, and continuum scales," Computer Physics Communications **271**, 108171 (2022).

[10] H. J. C. Berendsen, J. R. Grigera, and T. P. Straatsma, "The missing term in effective pair potentials," The Journal of Physical Chemistry **91**, 6269–6271 (1987).

[11] H. C. Andersen, "Rattle: A "velocity" version of the shake algorithm for molecular dynamics calculations," Journal of Computational Physics **52**, 24–34 (1983).

[12] T. Werder, J. H. Walther, R. L. Jaffe, T. Halicioglu, and P. Koumoutsakos, "On the water–carbon interaction for use in molecular dynamics simulations of graphite and carbon nanotubes," The Journal of Physical Chemistry B **107**, 1345–1352 (2003).

[13] A. Dequidt, J. Devémy, and A. A. H. Prádua, "Thermalized Drude oscillators with the LAMMPS molecular dynamics simulator," Journal of Chemical Information and Modeling **56**, 260–268 (2016).

[14] R. P. Misra and D. Blankschtein, "Insights on the role of many-body polarization effects in the wetting of graphitic surfaces by water," The Journal of Physical Chemistry C **121**, 28166–28179 (2017).

[15] R. Hockney and J. Eastwood, *Computer Simulation Using Particles* (Adam-Hilger, 1988).

[16] J. Kolafa and J. W. Perram, "Cutoff errors in the ewald summation formulae for point charge systems," Molecular Simulation **9**, 351–368 (1992).

[17] W. Shinoda, M. Shiga, and M. Mikami, "Rapid estimation of elastic constants by molecular dynamics simulation under constant stress," Phys. Rev. B **69**, 134103 (2004).

[18] M. E. Tuckerman, J. Alejandre, R. López-Rendón, A. L. Jochim, and G. J. Martyna, "A liouville-operator derived measure-preserving integrator for molecular dynamics simulations in the isothermal–isobaric ensemble," Journal of Physics A: Mathematical and General **39**, 5629–5651 (2006).

[19] L. Bocquet and J.-L. Barrat, "Hydrodynamic boundary conditions, correlation functions, and kubo relations for confined fluids," Phys. Rev. E **49**, 3079–3092 (1994).

[20] L. Bocquet, J.-P. Hansen, and J. Piasecki, "Friction tensor for a pair of brownian particles: Spurious finite-size effects and molecular dynamics estimates," Journal of Statistical Physics **89**, 321–346 (1997).

[21] P. Español, J. A. de la Torre, and D. Duque-Zumajo, "Solution to the plateau problem in the Green–Kubo formula," Phys. Rev. E **99**, 022126 (2019).

[22] G. Tocci, L. Joly, and A. Michaelides, "Friction of water on graphene and hexagonal boron nitride from ab initio methods: Very different slippage despite very similar interface structures," Nano Letters **14**, 6872–6877 (2014).

[23] A. R. Poggioli and D. T. Limmer, "Distinct chemistries explain decoupling of slip and wettability in atomically smooth aqueous interfaces," The Journal of Physical Chemistry Letters **12**, 9060–9067 (2021).

[24] H. Oga, Y. Yamaguchi, T. Omori, S. Merabia, and L. Joly, "Green–Kubo measurement of liquid-solid friction in finite-size systems," The Journal of Chemical Physics **151**, 054502 (2019).

[25] A. Savitzky and M. J. E. Golay, "Smoothing and differentiation of data by simplified least squares procedures." Analytical Chemistry **36**, 1627–1639 (1964).

[26] A. Seal and A. Govind Rajan, "Modulating water slip using atomic-scale defects: Friction on realistic hexagonal boron nitride surfaces," Nano Letters **21**, 8008–8016 (2021).

[27] L. Joly, G. Tocci, S. Merabia, and A. Michaelides, "Strong coupling between nanofluidic transport and interfacial chemistry: How defect reactivity controls liquid-solid friction through hydrogen bonding," The Journal of Physical Chemistry Letters **7**, 1381–1386 (2016).

[28] C. Rupakheti, G. Lamoureux, A. D. MacKerell, and B. Roux, "Statistical mechanics of polarizable force fields based on classical drude oscillators with dynamical propagation by the dual-thermostat extended lagrangian," The Journal of Chemical Physics **153**, 114108 (2020).

[29] G. Bussi, D. Donadio, and M. Parrinello, "Canonical sampling through velocity rescaling," The Journal of Chemical Physics **126**, 014101 (2007).

[30] J. C. Shelly, "Boundary condition effects in simulations of water confined between planar walls," Molecular Physics **88**, 385–398 (1996).

[31] J. Alejandre, D. J. Tildesley, and G. A. Chapela, "Molecular dynamics simulation of the orthobaric densities and surface

tension of water," The Journal of Chemical Physics **102**, 4574–4583 (1995).

[32] S. E. Feller, R. W. Pastor, A. Rojnuckarin, S. Bogusz, and B. R. Brooks, "Effect of electrostatic force truncation on interfacial and transport properties of water," The Journal of Physical Chemistry **100**, 17011–17020 (1996).

[33] C. Zhang and M. Sprik, "Computing the dielectric constant of liquid water at constant dielectric displacement," Phys. Rev. B **93**, 144201 (2016).

[34] C. Zhang and M. Sprik, "Finite field methods for the supercell modeling of charged insulator/electrolyte interfaces," Phys. Rev. B **94**, 245309 (2016).

[35] S. J. Cox and M. Sprik, "Finite field formalism for bulk electrolyte solutions," The Journal of Chemical Physics **151**, 064506 (2019).

[36] I.-C. Yeh and M. L. Berkowitz, "Ewald summation for systems with slab geometry," The Journal of Chemical Physics **111**, 3155–3162 (1999).

[37] Y. Wu, H. L. Tepper, and G. A. Voth, "Flexible simple point-charge water model with improved liquid-state properties," The Journal of Chemical Physics **124**, 024503 (2006).

[38] N. Kavokine, M.-L. Bocquet, and L. Bocquet, "Fluctuation-induced quantum friction in nanoscale water flows," Nature **602**, 84–90 (2022).

[39] J. M. Pitarke, V. M. Silkin, E. V. Chulkov, and P. M. Echenique, "Theory of surface plasmons and surface-plasmon polaritons," Reports on Progress in Physics **70**, 1–87 (2006).

[40] G. Tocci, M. Bilichenko, L. Joly, and M. Iannuzzi, "Ab initio nanofluidics: disentangling the role of the energy landscape and of density correlations on liquid/solid friction," Nanoscale **12**, 10994–11000 (2020).

[41] F. L. Thiemann, C. Schran, P. Rowe, E. A. Müller, and A. Michaelides, "Water flow in single-wall nanotubes: Oxygen makes it slip, hydrogen makes it stick," ACS Nano **16**, 10775–10782 (2022).

[42] Y.-l. Yeh and C.-Y. Mou, "Orientational relaxation dynamics of liquid water studied by molecular dynamics simulation," The Journal of Physical Chemistry B **103**, 3699–3705 (1999).

[43] A. Luzar and D. Chandler, "Hydrogen-bond kinetics in liquid water," Nature **379**, 55–57 (1996).